Photoacoustics 45 (2025) 100745

Contents lists available at ScienceDirect

Photoacoustics

journal homepage: www.elsevier.com/locate/pacs

Artifacts in photoacoustic imaging: Origins and mitigations

Max T. Rietberg [a,1], Janek Gröhl [b,c,e,1], Thomas R. Else [b,c,1], Sarah E. Bohndiek [b,c], Srirang Manohar [a,*], Benjamin T. Cox [d,*]

[a] Multi-Modality Medical Imaging, TechMed Centre, University of Twente, Drienerlolaan 5, Enschede, 7522 NB, Overijssel, The Netherlands
[b] Cancer Research UK, Cambridge Institute, University of Cambridge, Robinson Way, Cambridge, CB2 0RE, United Kingdom
[c] Department of Physics, University of Cambridge, JJ Thomson Avenue, Cambridge, CB3 0HE, United Kingdom
[d] Department of Medical Physics and Biomedical Engineering, University College London, Gower St, London, WC1E 6BT, United Kingdom
[e] ENI-G, a Joint Initiative of the University Medical Center Göttingen and the Max Planck Institute for Multidisciplinary Sciences, Grisebachstr. 5, Göttingen, 37077, Germany

ARTICLE INFO

Dataset link: https://gitlab.com/MTRietberg/artifact-paper

Keywords:
Medical imaging
Molecular imaging
Imaging artifacts
Radiology
Review

ABSTRACT

Photoacoustic imaging (PAI) is rapidly moving from the laboratory to the clinic, increasing the need to understand confounders which might adversely affect patient care. Over the past five years, landmark studies have shown the clinical utility of PAI, leading to regulatory approval of several devices. In this article, we describe the various causes of artifacts in PAI, providing schematic overviews and practical examples, simulated as well as experimental. This work serves two purposes: (1) educating clinical users to identify artifacts, understand their causes, and assess their impact, and (2) providing a reference of the limitations of current systems for those working to improve them. We explain how two aspects of PAI systems lead to artifacts: their inability to measure complete data sets, and embedded assumptions during reconstruction. We describe the physics underlying PAI, and propose a classification of the artifacts. The paper concludes by discussing possible advanced mitigation strategies.

1. Introduction

Medical imaging technologies enable visualization of the structure and function of biological tissues, thereby facilitating disease detection, diagnosis, monitoring of treatment response and follow-up. Medical imaging modalities rely on the measurement of transmitted, absorbed, scattered, or emitted energy of some form. Measured data and physical models of energy-tissue interactions are then used to reconstruct images [1]. These models necessarily involve simplifying assumptions, and so describe the true physical processes only approximately. Furthermore, during data collection some information will be lost, whether due to hardware limitations or subject and environmental factors. The reconstructed image will therefore not be a perfect representation of the underlying tissue but will contain deviations, called artifacts. An artifact is a structure, distortion, or feature in an image that does not correspond to the actual anatomical, morphological, physiological, or pathological reality of the imaged subject [2,3]. The presence of artifacts may confound clinical interpretation and negatively affect decision making. For example, artifacts include the obscuring, displacement or distortion of genuine structural or functional features, or the presence of features that are not real, perhaps giving the illusion of pathophysiology. Artifacts can lead to images being misinterpreted, errors in quantitative (e.g., molecular) information extracted from the image, and false positive or false negative imaging biomarkers. A thorough understanding of artifacts in medical imaging is therefore crucial to ensure reliable and accurate clinical use.

Artifacts can be especially prominent in multi-physics imaging modalities like photoacoustic imaging. In photoacoustic (PA) imaging (PAI) the acoustic emissions from the absorbed optical energy distribution are measured, in contrast to purely optical imaging methods such as diffuse optical tomography [4], where transmitted or reflected light is detected. In PAI, tissue is interrogated with nanosecond pulsed light, which is scattered and absorbed inside the tissue. The light is absorbed by chromophores, leading to a localized temperature and pressure rise, and subsequently, due to thermoelastic expansion, the emergence of acoustic pressure waves [5]. Detection of acoustic waves outside the tissue followed by image reconstruction enables visualization of the distribution of absorbed optical energy up to several centimeters deep. By varying the wavelength of incident light, absorption of several different molecules can be probed [6]. Typical features extracted from PAI with promise for clinical translation include (1) vascular architecture [7–9],

* Corresponding authors.
E-mail addresses: s.manohar@utwente.nl (S. Manohar), b.cox@ucl.ac.uk (B.T. Cox).
[1] Equal contribution.

https://doi.org/10.1016/j.pacs.2025.100745
Received 16 April 2025; Received in revised form 5 June 2025; Accepted 24 June 2025
Available online 5 July 2025

(2) signal intensity at a target wavelength [10–12], (3) blood oxygen saturation [13–15], (4) general molecular concentration information of, e.g., fatty tissue, glandular tissue, water [16,17], and (5) contrast agent distribution [18,19]. Photoacoustic image formation thus involves an interplay of optical, thermal, elastic and acoustic properties, and gives rise to a variety of unique artifacts not seen in optical or ultrasound imaging separately. The presence of artifacts can have negative effects on the qualitative and quantitative interpretation of PAI images and their extracted features.

In the context of PAI, we define an artifact as a feature in the image that does not correspond, spatially or spectrally, to the true anatomical, morphological and spectral characteristics of the imaging target under investigation.

As PAI is on the cusp of achieving clinical breakthroughs in various applications [20,21], we believe it would be helpful to raise awareness of artifacts in the PAI community, especially among the growing number of clinical PAI users. PA users should be able to identify artifacts, so they can better understand and improve the interpretation of *in vivo* PA images or even take advantage of the artifacts, as they could carry diagnostic information. Furthermore, we hope that recognizing artifacts and understanding their origins will help guide the development of PAI systems towards mitigations and hasten the progress towards improved PAI technology.

In this work, we structure the manuscript by the *sources* and *causes* of artifacts. Starting with a short description of the physics involved in PAI, we continue by outlining the reasons behind the emergence of each artifact, and briefly discuss possible mitigation strategies. Each artifact is demonstrated with simulated images and, where available, experimental examples. Simulations are performed on simple digital phantoms in which the assumptions made during image reconstruction are deliberately broken to demonstrate their confounding effect. For illustrative purposes, the simulations are restricted to simple but typical clinical PA detection geometries; however, similar artifacts would appear in other hardware configurations [22,23]. We conclude with a discussion of possible advanced artifact mitigation strategies.

2. Artifact classification

Necessary compromises in the design of PAI systems mean that most PA images contain artifacts. Taking a high-level view, there are two parts to any PAI system: hardware for data acquisition, and a method for reconstructing and displaying the images. There are two corresponding classes of underlying causes of artifacts: (1) insufficient data, e.g., limited array size or limited bandwidth, and (2) incorrect assumptions in the image reconstruction algorithm, e.g., inaccurate approximations to the physics of wave propagation or an overly simple model of the detector response.

In practical applications, there are often good reasons for designing an imaging system that measures incomplete data, or for developing an image reconstruction approach that makes inaccurate assumptions. First, there are *clinical requirements*. These are dictated by what the clinician or researcher needs to see, which requires the instrument to access the body part of interest with a sufficient field-of-view and resolution. Further challenges, such as restrictions on the clinical workspace, fitting around other devices, and patient safety and comfort, are also key considerations. Second, there are *physics constraints*, e.g., limited light penetration or acoustic attenuation that limit imaging depths. Third, there are *practical limitations*, which include the availability of resources (raw materials, fabrication facilities, computing hardware), financial costs of hardware and operation, or even intellectual property rights and market demand. Trade-offs must be made in imaging system design, leading to widely differing PAI systems from microscopes to large-area bowls for breast imaging.

Artifacts in PAI may be classified in many different ways. Our approach is to classify artifacts into five groups distinguished by the *source* of the artifact, namely:

1. Patient: artifacts resulting from subject movement and experimental conditions.
2. Light–Matter Interactions: artifacts arising from inaccurate assumptions about the interactions between light and tissue.
3. The Photoacoustic Effect: artifacts arising from inaccurate assumptions relating to the photoacoustic efficiency (the *Grüneisen parameter*).
4. Sound–Matter Interactions: artifacts arising from inaccurate assumptions about the interactions between sound and tissue.
5. Signal Detection: artifacts arising from shortcomings in acquiring data, leading to loss or distortion of information.

These artifact *sources* can be subdivided into what we call artifact *causes*, such as fluence decay or acoustic reflection. An overview is given in Fig. 1. In addition, artifacts can be sorted into different types categorized by their appearance in the image. One way to classify the *effects* of artifacts is: (1) dislocation: a shift or displacement of image features from their correct positions, (2) splitting: duplication or division of a single object or feature, (3) blurring of image features: loss of sharpness or detail in the image, (4) the emergence of clutter superimposed on the image: unwanted visual elements that appear over the image, and (5) the unexpected loss or systematic change of the signal: portions of the image data go missing or change consistently in a way not intended. See Tables 1 and 2 in the Supplementary information for the relationships between assumptions, the artifact *sources* and *causes*, and the *effects*.

3. PAI imaging physics

The following section describes the underlying physical principles which may be of interest to those interested in a deeper understanding. However, it can be skipped by readers who are primarily focused on a practical understanding of PA artifacts.

3.1. Light propagation and absorption

The behavior of light in scattering media such as human tissue can, for the most part, be described accurately by modeling light as a particle [5]. Modeling can be achieved using the radiative transfer equation, also called Boltzmann's transport equation for low-energy, monochromatic photons. The radiative transfer equation describes the light radiance, $\phi(\mathbf{x}, \hat{\mathbf{s}}, t)$, the rate of optical energy flow per unit area per unit solid angle in direction $\hat{\mathbf{s}}$ at position $\mathbf{x}$ at time t, and can be written [24] as in Eq. (1).

where c is the velocity of light in the medium, $q(\mathbf{x}, \hat{\mathbf{s}}, t)$ is a source of photons, μ_a is the optical absorption coefficient, μ_s is the optical scattering coefficient, and $\Theta\left(\hat{\mathbf{s}}, \hat{\mathbf{s}}'\right)$ is the scattering phase function (a probability density function describing how photons traveling in direction $\hat{\mathbf{s}}$ will scatter to direction $\hat{\mathbf{s}}'$). The radiative transfer equation does not take into account inelastic scattering, radiative losses, wave effects, polarization, ionization, or other photochemical reactions. The absorbed energy density within the tissue $H(\mathbf{x})$, due to the absorption of light, can be written as in Eq. (2).

where the inner integral is over all angles and the time integral is long enough so all photons have either been absorbed or left the tissue. The time and angle-integrated radiance, Φ, is called the fluence.

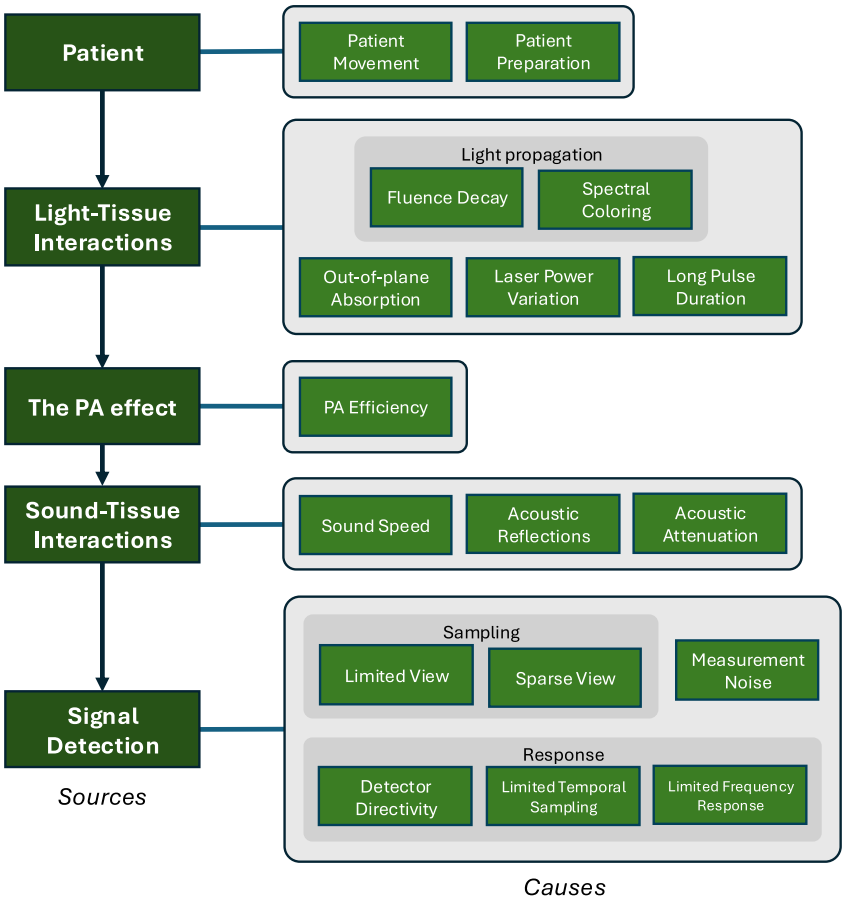

Fig. 1. Overview of the artifacts treated in this paper. They are arranged by the point at which they occur throughout the photoacoustic (PA) signal generation process: induced by (1) the patient or by the preparation of the patient; (2) the interactions of light with tissue; (3) the conversion of heat into sound energy; (4) the interactions of sound with tissue; (5) the detection of the sound waves.

Change in radiance over time
Light source
Absorption and scattering away from direction $\hat{\mathbf{s}}$

$$\frac{1}{c}\frac{\partial \phi(\mathbf{x},\hat{\mathbf{s}},t)}{\partial t} = q(\mathbf{x},\hat{\mathbf{s}},t) - \hat{\mathbf{s}}\cdot\nabla\phi(\mathbf{x},\hat{\mathbf{s}},t) - \left(\mu_a(\mathbf{x})+\mu_s(\mathbf{x})\right)\phi(\mathbf{x},\hat{\mathbf{s}},t) + \mu_s\int \Theta\left(\hat{\mathbf{s}},\hat{\mathbf{s}}'\right)\phi\left(\mathbf{x},\hat{\mathbf{s}}',t\right)\mathrm{d}\hat{\mathbf{s}}', \tag{1}$$

Change in radiance over space
Scattering into direction $\hat{\mathbf{s}}$ from other directions

Absorbed energy density
Optical absorption coefficient

$$H(\mathbf{x}) = \mu_a(\mathbf{x})\cdot\int\int \phi(\mathbf{x},\hat{\mathbf{s}},t)\mathrm{d}\hat{\mathbf{s}}\,dt = \mu_a(\mathbf{x})\cdot\Phi(\mathbf{x}), \tag{2}$$

Radiance integrated over direction $\hat{\mathbf{s}}$ and time t

3.2. Photoacoustic effect

The deposition of optical energy as heat in the tissue gives rise to local increases in temperature and pressure. When the pulse of light, and its subsequent absorption and thermalization, occurs on a timescale τ_p that is much shorter than the characteristic thermal relaxation time, the condition called *thermal confinement* is satisfied: $\tau_p \ll \tau_h = d_c^2/\alpha$, where d_c is the desired spatial resolution and α is the thermal diffusivity. A more stringent requirement is that the optical pulse is shorter than the acoustic relaxation time, which is called the *stress confinement*, $\tau_p < \tau_s = d_c/v$, where v is the sound speed. Satisfying these conditions means that pressure changes are dissipated as pressure waves and the acoustic propagation can be modeled as an initial value problem, where the initial acoustic pressure distribution, $p_0(\mathbf{x})$, is given as in Eq. (3).

where Γ is the PA efficiency, which is equal to the *Grüneisen parameter* for a pure optically-absorbing fluid. In this case, the efficiency depends on the tissue's thermomechanical properties, specifically the thermal expansion coefficient β, isothermal compressibility K_T, specific heat capacity C_p, and mass density ρ, as given in Eq. (4).

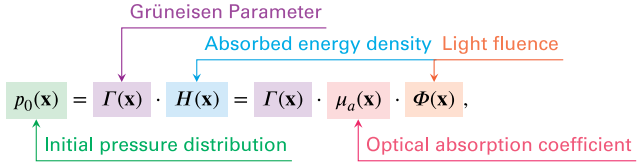

(3)

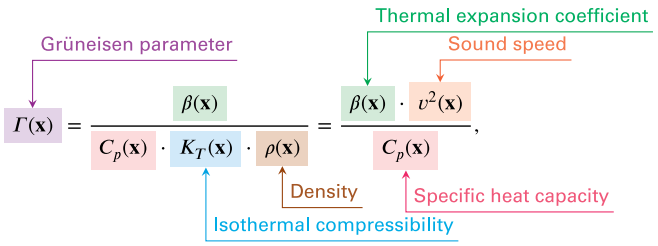

(4)

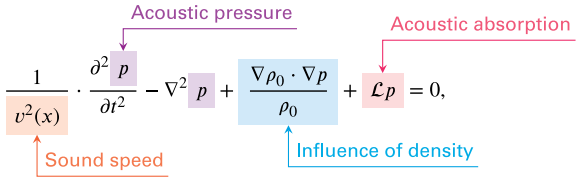

(5)

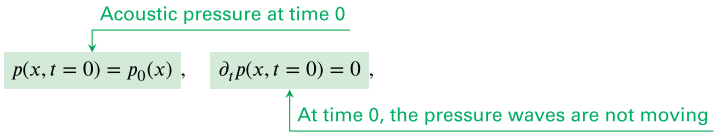

(6)

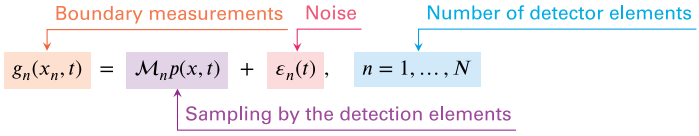

(7)

where $K_T = 1/\rho v^2$, with v as the sound speed. It should be noted that the PA efficiency is typically assumed constant and spatially uniform.

3.3. Acoustic propagation and detection

Photoacoustically generated waves are of sufficiently low amplitude that they can be modeled using linear acoustic theory. The PA initial value problem can therefore be written using the wave equation for heterogeneous media (see Eq. 5, 6 and 7).

where $p(x, t)$ is the acoustic pressure in tissue with sound speed v and mass density ρ_0. A variety of forms have been proposed for the absorption loss operator $\mathcal{L}$. The N measured time series $g_n(x_n, t)$ are recorded at the N detector points x_n via the measurement operators $\mathcal{M}_n$. ε_n represents noise. This mathematical model assumes the target is stationary on an acoustic time scale. However, if the measurements are not made simultaneously but sequentially with multiple excitation pulses, as is seen in some experimental systems, it might be that each measurement g_n is generated by a slightly different initial pressure distribution $p_{0,n}(x)$, e.g., if the tissue moves between laser excitation pulses. With the notation introduced here, many of the various assumptions typically made during image reconstruction can be written succinctly: spatial invariance of the tissue properties, e.g., $\nabla v = 0$, $\nabla \rho_0 = 0$, $\mathcal{L} = 0$, $\nabla \Gamma = 0$, or fluence approximations, e.g., $\nabla \Phi = 0$, or $\Phi(x) = \exp(-ax)$, or no tissue motion $p_{0,n} = p_0$, or assumptions about the detection process, such as that $\mathcal{M}$ is omnidirectional or has a flat frequency response.

4. Artifacts in PAI

The following sections will discuss artifacts encountered in PAI, grouped by source (Fig. 1). Each artifact will be explained and illustrated by a figure that demonstrates its origin through simulations, accompanied by experimental data whenever possible. The simulations are performed using SIMPA [25], see https://gitlab.com/MTRietberg/artifact-paper for our code.

In order to isolate particular artifacts, the simulations are (unless otherwise noted) performed in ideal settings, but for the one difference giving rise to the artifact. The ideal settings are: no patient movement, short enough laser pulse (satisfying the thermal and stress confinements for the imaged structures), no pulse-to-pulse laser power variation (50

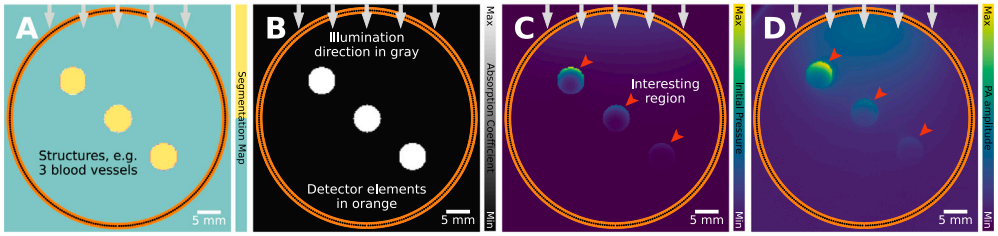

Fig. 2. A visual guide of how we will showcase visual explanations of the artifacts. In this example, three vessels are used and we typically showcase different types of views. **A**: the segmentation map (a segmented color bar shows the considered tissue types). **B**: the absorption coefficient in a gray-scale color map. **C**: the initial pressure and in **D**: the reconstructed image, both with a pseudo-colored visualization using the *Viridis* color mapping. In other figures, only the relevant components will be shown, e.g., only the absorption coefficient and the reconstructed image. In all figures, the illumination direction is denoted with gray arrows, the detector elements in orange (which appear in this figure as a continuous line due to the high detector density), and the scale with a scalebar at the bottom right corner. Noteworthy regions are indicated with red arrowheads. In addition to these plots, we also show reprinted examples from the literature, where possible.

mJ), all medium properties homogeneous (constant, the same everywhere), no acoustic attenuation, complete data collected by enclosing the region-of-interest with a ring-shaped transducer array with a high detector element density, detector elements with omnidirectional and broadband sensitivity, no added noise in both initial pressure and time series, and sufficient temporal sampling (40 MHz). The only artifact cause that is consistently present throughout all simulations is fluence decay, as the resulting artifact is unavoidably present in all PA images. The optical part of the simulation is performed in 3D (three spatial dimensions) and the acoustic part in 2D, with the exception of the out-of-plane absorption artifact where both the optical and the acoustic parts are performed in 3D. 2D acoustic simulations in k-Wave assume invariance with respect to the out-of-plane axis, essentially pretending that the signals infinitely repeat in that axis, reducing computational overheads with only a slight reduction in realism compared to full 3D simulations. The assumption is reasonable for the purposes of this work, since we merely aim to illustrate how artifacts can manifest. However, it should be noted that in general, when making comparisons with measured data for example, 3D simulations should be used. The volume is 50x50x50 mm, with a resolution of 0.25 mm/pixel. The default delay and sum beamforming algorithm from SIMPA is used [26], as delay and sum is widely used and relatively simple. Reconstruction techniques can incur artifacts themselves, e.g., time reversal can trap artifacts that would otherwise lie outside the image region [27], but discussion of these artifacts is outside the scope of this paper. An example figure with labels is shown in Fig. 2.

5. Artifact source: Light-tissue interactions

The interactions of light with tissue form the first part of the multi-physics process of photoacoustic signal generation, where several artifacts have their origin. Light scatters strongly in biological tissues and photons stochastically get absorbed along their travel paths, leading to signal changes. Propagation of photons in three spatial dimensions also leads to pressure buildup outside of the imaging plane. Furthermore, changes in the laser intensity will change the intensity of the PA image, and finally, the PA effect, which is governed by thermal and stress confinement conditions, and the duration of the light pulse can drastically change the appearance of the generated PA signal.

5.1. Fluence decay

The pressure amplitude of the PA waves generated by a chromophore is directly proportional to both the absorption coefficient and the light fluence (Eq. 2). As the illumination beam propagates in tissue, the scattering and absorption of photons cause a subsequent decrease in the light fluence and thus PA signal intensity with depth (Eq. 1). Additionally, strong absorption by discrete structures can form so-called shadows behind them, resulting in a lower PA signal intensity. In the diffuse regime of photon travel, there are typically no hard shadows observed, but an exponential decrease in the light fluence with imaging depth (i.e., fluence decay) is visible. We can distinguish three qualitatively different effects of fluence decay:

1. The gradual decay of fluence across the photon travel distance (typically imaging depth).
2. The rapid decay within a large absorbing object such that the center is less visible.
3. Optical shadowing, where multiple absorbers lie close to each other and mutually influence the fluence.

We designed the example shown in Fig. 3 in a way that all three effects of this artifact can be seen in the reconstruction (Fig. 3**B**). The vessel in the first row clearly shows the rapid decay of signal from the boundary to the core. In the second row, we see two vessels that have different signal amplitudes, caused by the asymmetrical absorption of photons of the vessel in the first row. The vessels in the third row are barely visible, highlighting the gradual decay of fluence with depth.

Fluence decay is present in nearly all PA images, and if not addressed can lead to over-estimation of PA signals or even under-estimation when incorrectly treated. However, the correction of fluence decay is complicated due to the nonlinear behavior and ill-posed nature of the inverse problem [29]. A simple mitigation that is commonly applied in practice is to use an exponential gain to the image, either radially or with depth. The exponential gain can be based on estimated optical tissue properties, e.g., the effective attenuation coefficient μ_{eff}, but will also amplify noise and thus not significantly increase the signal-to-noise ratio.

5.2. Spectral coloring

One can form PA images from a single excitation wavelength, but the true diagnostic power of PA lies within the possibility of multi-wavelength imaging. Performing multi-wavelength imaging provides a *PA amplitude* spectrum for each spatial point in the image, which can (in theory) be used to extract molecular and functional information of the imaged tissue. During linear spectral unmixing to match the PA amplitude spectrum with the absorption coefficient spectrum of target molecules, it is typically assumed that a PA spectrum is proportional to the absorption coefficient spectrum at a point [30]. Eq. 3, however, shows that the PA amplitude depends on the local fluence, which is not constant inside tissue. Instead, the fluence suffers a decay in tissue (Section 5.1). Furthermore, the scattering coefficient and especially the absorption coefficient are wavelength dependent, so that the fluence could experience marked reductions at selected spectral bands. The light reaching the structure is thus "colored" or filtered by the intervening tissue. Hence the name: spectral coloring. The PA spectrum from a certain location is then a distorted version of

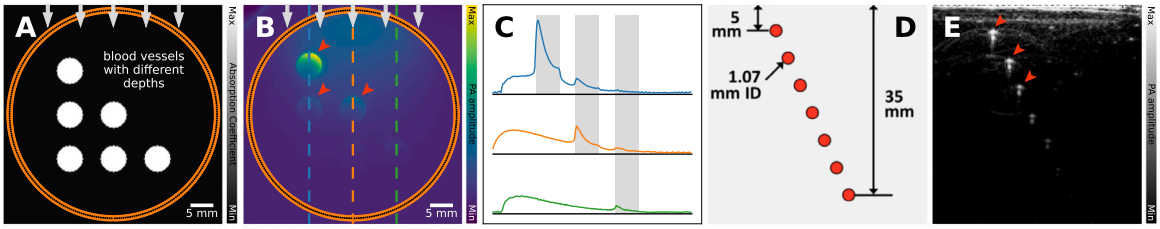

Fig. 3. Fluence decay artifact: leads to signal loss with depth. Several blood vessels are embedded in soft tissue, with increasing distance from the illumination source (increasing depth). **A**: their absorption coefficients. **B**: The fluence decays due to absorption from both the background and the blood vessels themselves, resulting in differing PA signal levels in the reconstruction. **C**: vertical intensity profiles taken from the reconstruction from **B** (denoted in dotted line in **B**), showing fluence decay. This can also be seen in experimental data. **D**: bovine blood-filled tubes, embedded in polyvinyl chloride plastisol, **E**: PA measurement with 800 nm. Just like our simulated example, tubes closer to the measurement surface result in a higher intensity than those deeper. The images in **D** and **E** have been reprinted from Vogt et al. 2019 with permission from the publisher [28]. The experimental data were captured with a linear transducer array and a laterally attached laser fiber bundle.

the correct spectrum expected from that location, i.e., spectral coloring describes the preferential absorption of light at shorter wavelengths as a spectrum of light travels through the tissue.

Spectral coloring can be seen in Fig. 4. At 763 nm, both without and with background absorption, the blood vessels are clearly visible (Fig. 4**E**&**F**). However, while the absorption coefficient of blood is higher at 1000 nm, the blood vessels are less visible (Fig. 4**G**). This difference can be attributed to the changing absorption coefficient of the background: the PA signal of the object under study is dependent on both the absorption spectrum of the object itself but also the background. This can also be seen in experimental results. The reference absorption spectra of water, melanin, HbO_2, Hb and fat differ a lot (Fig. 4**I**), which are chromophores expected to be present in the breast. We also see the spectral evolution of PA intensity in the RF signal from a single detector in the PAM3 breast imaging system (Fig. 4**J**). The PA intensities labeled 'water', 'skin' and 'T1' correspond to parts of the RF signal which are predominantly coming from water, skin and inside the breast respectively (see inset for a schematic). It can be seen that while the PA spectrum for water matches the reference spectrum, the PA spectrum measured from skin shows the melanin reference spectrum modulated by absorptions coming from other chromophores. The effect is more significant in the PA spectrum 'T1' where local dips in the spectrum match the absorption peaks of presumably the blood and fat contents of intervening tissues.

Correction for spectral coloring can, in theory, be done by correcting for fluence decay at each optical wavelength, but it is very difficult to achieve in practice since accurate modeling of the fluence requires accurate knowledge of the optical properties in the first place. An additional option to mitigate the fluence effect is to reduce the distance between the light source and target, such as in interstitial illumination [31,32], or in the endoscopic imaging settings where it occurs naturally [33]. A more practical mitigation approach is to solely look at relative changes in a derived functional biomarker [34], on the assumption that the fluence will not significantly affect the relative change. Another approach is to restrict the analysis close to the tissue surface or to the pixels with maximum intensity projection (e.g., in Kirchner et al. [35]), under the assumption that uncolored light dominates these regions.

5.3. Out-of-plane absorption

In 2D PAI using, e.g., a linear array or a ring array, it is often assumed that all detected PA signals originate from this plane, i.e., only absorbers in this slice of the tissue are excited. In practice, the highly optically scattering nature of tissue means that PA signals can be generated outside of the region of interest and be detected within the same time series. Detected signals from outside the imaging region are then projected inside the region during reconstruction. Fig. 5 shows where the addition of a sphere outside the imaging plane appears in the reconstructed image. Such artifacts can partly be corrected by changing from a 2D transducer array and reconstruction technique to 3D variants or increasing the directionality of the transducer elements. Furthermore, in real-time handheld PA devices, the situation could be ameliorated by the operator moving the image plane slightly to see that there is an absorber out-of-plane.

5.4. Laser power variation

In certain cases, a single measurement is not sufficient to create a PA image. For example, in raster-scanning systems (e.g., linear or rotating) and when making multi-wavelength measurements. When imaging a subject multiple times, the assumption is often implicitly made that all changes between frames originate from within the subject (e.g., heartbeat). However, if the laser pulse-to-pulse power is not stable over time, the resultant signal will change, even if everything else remains the same. If not corrected, laser power variations lead to global changes in the measured PA signal across illumination wavelength and time, hampering image quantification. Fortunately, correction of fluctuating laser power is routinely done via hardware solutions, and static wavelength-dependent changes can be calibrated for before the measurements. The choice of type light source can also have an impact on the stability of the pulse-to-pulse power. For instance, optical parametric oscillators (OPOs) are known to have higher fluctuations compared to more stable sources such as Nd:YAG lasers or LEDs. For live measurements of the laser power during acquisition, a beamsplitter is typically used to redirect a small percentage (e.g., $< 1\%$) of the total light to another sensor. The artifact is visualized in Fig. 6, where three blood vessels are imaged with varying laser power.

5.5. Long pulse duration

Illumination in PAI is most commonly achieved via a pulsed laser. The length of the laser pulses can be as low as femtoseconds [38], but in the context of PAI these typically have a duration of 5 to 10 ns. These pulses should be short, such that the thermal and stress confinement conditions are fulfilled [5], and have sufficient pulse energy, while avoiding potential damage to tissue. Violating the confinement conditions with a longer pulse duration acts as a low-pass filter, meaning that no high acoustic frequencies are generated, resulting in blurry PA images, where features can be obscured. The effect of an extended duration pulse can be seen in Fig. 7, where an increasing pulse duration creates artifacts. Since the pulse length is a relatively stable property of the imaging system, pulse length artifacts are uncommon when imaging with commercially available, clinically approved systems. However, this artifact may become noticeable with the increasing uptake of light-emitting diode and laser diode illumination systems for clinical devices, which require longer pulses to compensate for their lower output power [39,40]. Mitigation approaches used are often deconvolution-based deblurring [41], which uses the fact that the degraded, detected signal is the result of a time convolution with the ideal PA signal and the laser pulse.

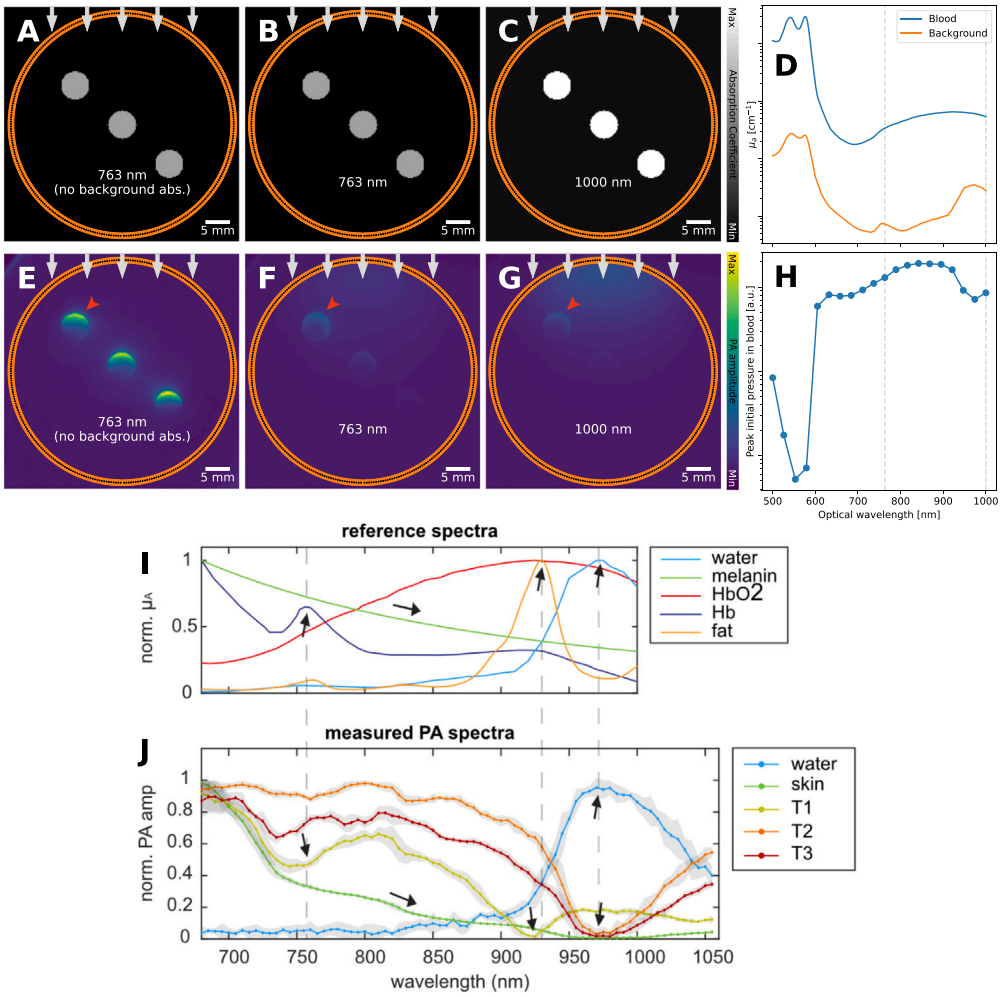

Fig. 4. Spectral coloring artifact: leads to unexpected signal difference between wavelengths. 3 blood vessels are embedded in soft tissue and imaged. **A&E**: 763 nm, no background absorption, **B&F**: 763 nm, **C&G**: 1000 nm. **A–C**: absorption coefficients. **E–G**: reconstruction. As an extension of the fluence decay artifact, the PA signal of the object under study is dependent on both the absorption spectrum of the object itself but also the background. In **E**, the blood vessels are clearly visible. In **F**, the light is being absorbed at the surface meaning that the blood vessels are less visible (i.e., fluence decay). However, even though the absorption coefficient of blood in **C** (1000 nm) is higher than in **B** (763 nm), the blood vessels are even less visible, as the background has also increased in absorption coefficient and thus has absorbed more light. **D**: the absorption coefficient against the optical wavelength (with the wavelengths from **B&C** highlighted), and **H**: peak initial pressure against optical wavelength. This can also be seen in experimental data, such as the one shown in **I** and **J**. **I**: the reference absorption spectra, and **J**: the measured PA spectra (corrected for pulse energy and normalized) of several locations around or in a healthy breast (water in the imaging bowl, T1, T2, T3 are points lying deeper in the breast). In **J** one can see the effect of the spectral coloring, e.g., T1 has a local minimum at 755 nm which corresponds to a peak in the reference spectrum of Hb. The *in vivo* graphs in **I** and **J** have been reprinted from Dantuma et al. 2023 [36], which is available open-access under a CC BY 4.0 license.

6. Artifact source: The photoacoustic effect

The PA efficiency Γ (Eq. 3) is a material property that quantifies the pressure increase, p_0, resulting from the deposited thermal energy, originating from light absorption and non-radiative de-excitation [5, 43]. The PA efficiency is defined for the medium where light absorption and pressure wave generation occur. In most biological tissues, blood dominates PA signal generation due to the strong optical absorption of hemoglobin in red blood cells. In such cases, under the confinement regimes the PA efficiency is primarily a property of blood rather than the surrounding tissue.

PA signals can also originate from tissue types other than blood, if they have sufficiently high optical absorption at the illumination wavelength [44]. When non-blood tissue components directly absorb light, their own PA efficiency governs the PA signal. Organs are inherently heterogeneous, consisting of different tissues such as muscle, adipose tissue, connective tissue, tumors, and fluid-filled lesions. Even though these different tissues clearly have varied molecular composition, it is often implicitly assumed that the PA efficiency is spatially uniform within an organ or tissue region. This assumption can lead to inaccuracies and artifacts in quantitative PAI, as the PA signal strength depends not only on the absorbed energy density but also on spatial variations in the PA efficiency, which can be seen in Fig. 8.

An often overlooked factor is that the PA efficiency is temperature-dependent [5,45]. The PA efficiency may thus not be constant under different physiological or experimental conditions, which can introduce additional uncertainty where temperature effects are significant and has in fact shown promise in applications for thermal therapy monitoring with PAI [46–49]. The PA efficiency can also be concentration-dependent, although this typically only manifests in a problematic sense in copper and nickel sulfate solutions used in phantoms [50].

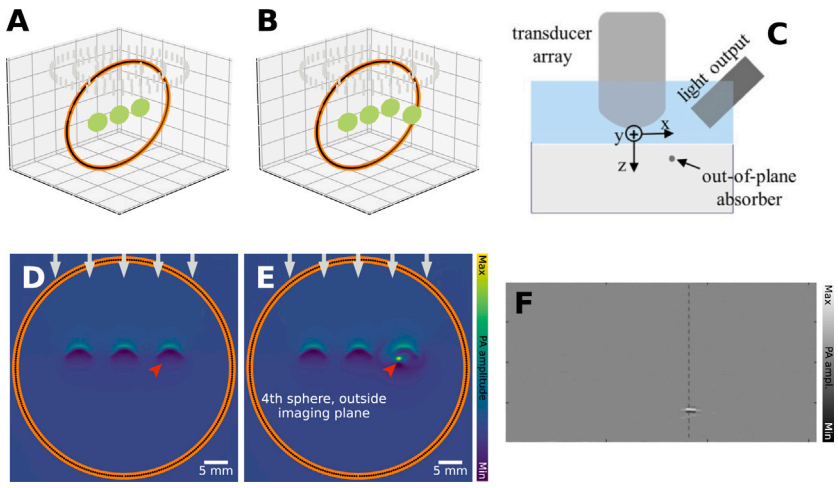

Fig. 5. Out-of-plane absorption artifact: leads to clutter. The assumption is that only tissue in the imaging plane or volume is illuminated, as in the case in **A**&**D**, where 3 objects are imaged. The second column (**B**&**E**) shows the same case, but now with a 4th object outside the imaging plane that is illuminated, which is reconstructed inside the imaging plane. **A**&**B**: segmentation map, and **D**&**E**: reconstruction. This can also be seen in experimental data, such as the one shown in **C**&**F**. **C**: measurement configuration, where an absorber is placed out-of-plane (imaging plane is along Y-Z). **F**: reconstructed image, where the absorber is erroneously shown inside the imaging plane. The experimental images have been reprinted from Nguyen et al. 2020 [37], which is available open-access under a CC BY-NC-ND 4.0 license. The dotted line is part of further analysis in the original source and not relevant here.

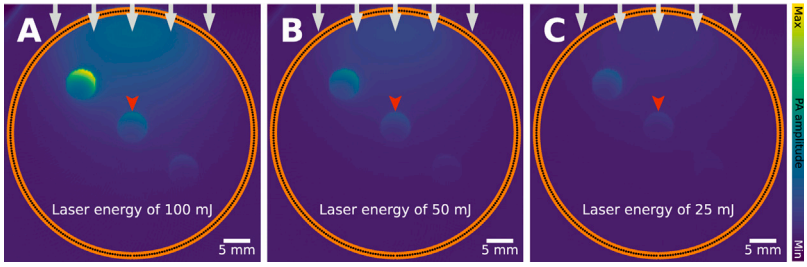

Fig. 6. Laser power variation artifact: leads to unexpected signal difference. It is often assumed that the laser power is constant between measurements, which might not always be the case. Three blood vessels are measured in identical settings, except the laser power varies, resulting in change in PA signal. **A**: laser energy of 100 mJ, **B**: 50 mJ, **C**: 25 mJ, all at 5 ns pulse duration.

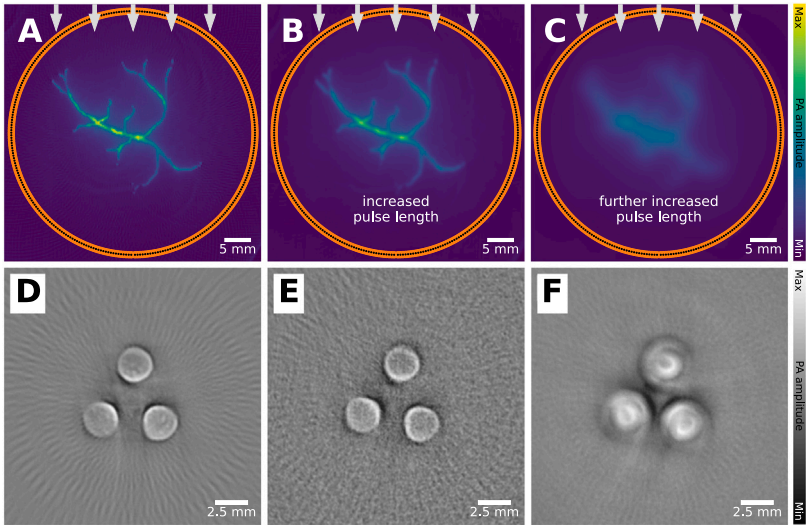

Fig. 7. Long pulse duration artifact: leads to blurring. If the laser pulse is not short enough, confinement conditions are violated and PA signal is distorted. **A**: when imaging with a short enough pulse, the reconstruction is not distorted, **B**: increasing the pulse length will distort the reconstruction, **C**: further increases the pulse length will distort the image even more. This can also be seen in experimental data. **D–F** show measurements on three cylindrical absorbing elements inside a scattering gel, measured with **D**: 7, **E**: 65 and **F**: 500 ns pulse duration. In **A–C**, the effect of the pulse duration is emulated through convolution with a Gaussian function. The experimental images have been reprinted from Allen et al. 2006 with permission from the publisher [42]. The experimental data were captured with a single transducer element covering a full circular array configuration with a single laser fiber delivering the light from the top.

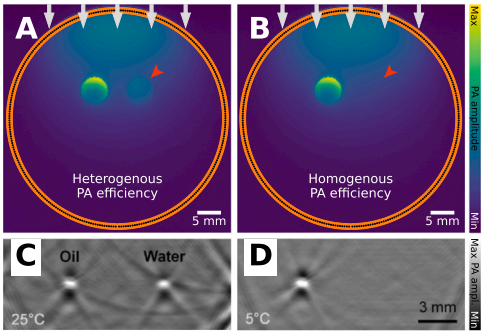

Fig. 8. PA efficiency artifact: leads to unexpected signal difference. Often, PA efficiency is assumed to be homogeneous, but this may not always be the case. **A**: a PA image of a blood vessel (left) and fat blob (right) with heterogeneous PA efficiency coefficient (0.2004 for blood and background, 0.8 for fat), **B**: a PA image with homogeneous, 0.2004, PA efficiency coefficient. There is a clear difference in intensity, which is not the result of a changing absorption coefficient, but of a changing PA efficiency. This can also be seen in experimental data, where two tubes filled with mineral oil and pure water are imaged with PAI, imaged at **C**: 25°C and **D**: 5 °C. The change in temperature results in a difference in PA efficiency. The experimental images have been reprinted from Petrova et al. 2017 [55], which is available open-access under a CC BY-NC-ND 4.0 license. The experimental data were captured with a linear transducer array and two laterally attached laser fiber bundles.

Assumptions regarding spatially uniform PA efficiency can be further confounded by the use of nanoparticle-based PA contrast agents, whereby the acoustic wave generation arises due to the rapid transfer of heat from the nanoparticles to the surrounding fluid: an *indirect photoacoustic effect*. In such a setting, the absorption coefficient, mass density and specific heat capacity would be those of the particles, but the thermal expansion coefficient and the isothermal compressibility would be those of the surrounding medium. In other words, the nanoparticle serves as a local heater, but the thermoelastic conversion into a pressure wave occurs in the surrounding medium [51–54]. This phenomenon could introduce complexities in quantitative PAI, as the measured signal depends not solely on the imaging target (the nanoparticle).

7. Artifact source: Sound-tissue interactions

When reconstructing PA images from measured data, it is necessary to know the acoustic properties of the medium, in particular the sound speed. Although the acoustic properties of biological tissue usually vary across the field of view, but in general, a map of the acoustic properties is not available. For this reason, and because for soft tissue it is a reasonable starting assumption, used widely in ultrasound, the acoustic properties are commonly treated as though they are spatially homogeneous, and each is defined by a single value. Although this can be a good approximation, especially for small regions of soft tissue, when it fails, artifacts appear in the PA images as a consequence.

7.1. Sound speed

Accurate PA image reconstruction relies on being able to map measured time series back into the spatial domain through knowledge of the sound speed. To help visualize how inaccuracy in the sound speed can affect PA images, consider the simple case of a point-like PA source that emits a spherical pulse of sound in a medium with a constant sound speed v. For the simple case of a point-like PA source, variations in sound speed will impact the pulse of sound emitted isotropically, and due to interactions such as reflection, diffraction, and scattering, the pulse will also not necessarily travel along a straight path between the source and detector. In other words, sound speed heterogeneities can change the time it takes acoustic waves to reach the detectors as well as bend or scatter them. When the image reconstruction algorithm neglects these effects by assuming a homogeneous sound speed, artifacts will result, which can be seen in Fig. 9.

In the simulated examples (Fig. 9**A**&**B**), a vascular network is imaged under the assumption that the sound speed is constant when it contains a region with slightly different sound speed surrounding the target region, reflecting an imaging scenario in which the object (such as a breast or small animal) is surrounded by water as a coupling medium. Ignoring the difference in the sound speed can lead to characteristic splitting and blurring artifacts. This is also visible in the experimental example (Fig. 9**C**&**D**), an *in vivo* example of breast imaging [36], in which two deep-lying vessels, which are visible in the image when the spatial variation in the sound speed distribution is taken into account, are not visible when the image is reconstructed assuming a constant sound speed.

When the detection array surrounds the object (Fig. 9**A–D**), the effect on the image of the distortions that the PA waves accumulate as they travel across the whole imaged region can be mitigated by reconstructing the image using only the first half of the time series data, up to time R/v, where R is the radius of the detection array [56]. However, this is not possible for many PA scanner geometries. A useful but non-optimal approach to mitigating a non-uniform sound speed is to continue to assume a homogeneous sound speed but to optimize the value of the sound speed in some way [57–60]. For some measurement setups, it is feasible to obtain sound speed estimates from complementary measurements, such as reflection ultrasound measurement in a circular array configuration [61], or pulse-echo sequences using handheld ultrasound geometries [62]. Advanced mitigation strategies would entail the simultaneous reconstruction of initial pressure and sound speed from the PA measurements [63].

7.2. Acoustic reflections

Heterogeneous speed of sound or density across the field of view can affect image reconstruction in two ways: firstly, scattering can attenuate the PA signals, and secondly, waves scattered from the primary PA waves may themselves be of sufficient amplitude to be detected and thereby result in clutter artifacts in the images. Clutter is more likely when the scatterer is large compared with the PA pulse. One important case is when the primary PA waves are generated in the skin through absorption by melanin [64,65]. Clutter has also been reported from PA waves generated at the face of the detector array itself [66,67].

This artifact is demonstrated in Fig. 10. A vascular target is imaged through a medium with background sound speed 1540 m/s and a circular region with high sound speed of 1800 m/s (Fig. 10**A**&**B**). Here, the heterogeneous region acts as a strong scatterer, and the clutter artifacts that result from this scattered part of the signal not being mapped back into the correct region in the image are clearly visible. In a different case, the scatterer is a bone layer lying parallel to the vessel of interest (Fig. 10**C**&**D**). Here, the reflection from the bone appears in the image as another linear feature at twice the blood-bone distance. Reflection artifacts are also visible in the *in vivo* example (Fig. 10**E**), showing reflection artifacts in an image of a papillary thyroid carcinoma

In some simple cases, it may be possible to mitigate the presence of reflected signals by time-gating in the raw time series. For example, this would be possible in the linear example (Fig. 10**C**&**D**) as the reflections will arrive later than the primary PA signal.

7.3. Acoustic attenuation

As PA waves travel through tissue, they are scattered to some extent. While scattering from large scatterers can result in discrete measurable reflections, as discussed above, the main effect of scattering from small scatterers (diffuse or Rayleigh scattering) is to attenuate the primary PA waves, an effect that increases strongly as a function of frequency. In addition, acoustic absorption (conversion of acoustic energy to heat) will occur in biological tissues and also increases strongly with frequency. Attenuation (used here as an umbrella term to include the

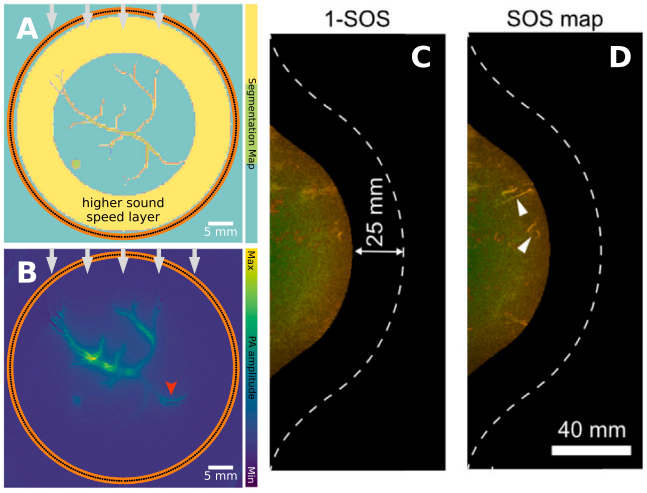

Fig. 9. Sound speed artifact: leads to dislocation, splitting, and blurring. **A&B**: Simulation showing the effect of a sound speed heterogeneity when imaging a vascular network assuming constant background sound speed. **A**: Schematic of the vascular target with background sound speed 1540 m/s, yellow annulus 1580 m/s. **B**: Image corresponding to **A** showing splitting and blurring artifacts due to the time delays introduced by the region of higher sound speed. **C&D**: Maximum intensity projections of *in vivo* PA breast images, **C**: reconstructed assuming constant sound speed, and **D**: using a 3D measurement of the sound speed distribution obtained using ultrasound tomography. In both cases, the outermost 25 mm of tissue is not shown so that deeper vessels are visible and not obscured by more superficial vessels. The white dashed line marks the surface of the breast. The arrowheads indicate vascular structures that are lost under the assumption that the sound speed is constant. The *in vivo* images are reprinted from Dantuma et al. 2023 [36], under a CC BY 4.0 license). The experimental data were captured with a custom hemispherical cup design, where transducer elements and laser fiber outputs are regularly distributed.

effects of both scattering and absorption) therefore decreases the PA signal amplitude and SNR with depth, preferentially removing the higher frequencies. The result is a decrease in the image resolution since ultrasound frequency defines the axial and lateral resolution of the image. This can be seen in Fig. 11, in which the presence of an absorbing region attenuates the signals traveling through it. As absorption in tissue more strongly attenuates higher frequencies, the waves from the center of the image, which have traveled furthest, have the highest frequency content removed, hence vessels near the center of the image are blurred. The effect of acoustic attenuation can be ameliorated through deconvolution to some extent if its frequency-dependence is known [68], although when the signal has fallen into the measurement noise, it cannot be recovered.

8. Artifact source: Signal detection

The previous sections discussed sources of artifacts caused by the difference between the true physical interactions of light and sound with tissue and the assumptions made in the image reconstruction. This section will discuss limitations in the acoustic signal detection hardware that can lead to an insufficient capture of PA pressure waves, introducing artifacts into the reconstructed images because of a lack of data. These artifacts arise from: (1) sampling of the acoustic field, as we can only have discrete measurement points, which are subject to the arrangement and pose of the transducer elements in 3D space and temporal sampling of the acoustic pressure, (2) the response of the detector elements, as acoustic detectors respond differently to the incoming acoustic pressure depending on the frequency of the waves and the incident angle, and (3) noise, as measurements are subject to electrical and thermal effects.

8.1. Sampling of the acoustic field

PAI scanners have been implemented in various configurations, catering to the application's requirements [69]. Pre-clinical PA scanners for small animal imaging, can typically be found in a tomographic imaging setting, optimized for slice-wise imaging through the specimen with full angular coverage (Fig. 12**A**, e.g., [61]), sometimes with a sparsely populated arrays (Fig. 12**B**, e.g., [70]), or with reduced angular coverage (Fig. 12**C**, e.g., [71]). Most clinical PAI scanners, on the other hand, are operated in a handheld mode, similar to conventional ultrasound scanners. These record 2D image slices and have either limited angular coverage (Fig. 12**C**, e.g., [72]) or are even used with a linear detection array (Fig. 12**E**, e.g., [73]).

There exist scanners with other geometries as well. One example is an L-shaped detector (Fig. 12**D**, e.g., [74]) that can reconstruct a greater field of view by placing a second linear array orthogonal to the first. Another example is a three-dimensional hemispherical detector array that can be used for breast imaging [75], or 3D tomographic preclinical imaging [76]. For endoscopic [33], mesoscopic [77], or microscopic [78] PAI, single detectors are often used. When using a single detection element, images can be reconstructed by mechanical scanning (translating and rotating a singular detector in space) or by optical scanning (deflecting the excitation laser across the tissue).

8.1.1. Limited view

In the limited view problem, a *visible region* can be defined, wherein objects present can be reconstructed accurately. This visible region represents the area from which acoustic signals can reach the detector array over a wide range of angles. The visible region can be visualized schematically, as the envelope of the detection curve (2D) or surface (3D).

This visible region is indicated in blue in Fig. 12. In a 3D setting, any object in the visible region can (in theory) be reconstructed accurately, and in 2D, its edges can be reconstructed accurately [79,80]. On the other hand, if the imaging target is outside of the visible region, it leads to characteristic artifacts that depend on the detection geometry and the employed reconstruction algorithm in Fig. 13.

Strictly speaking, linear arrays provide zero angular coverage for most directions other than those orthogonal to the array. This technically results in a very limited or even zero visible region. In practice, reconstructions are still performed, but they are affected by the limited-view artifacts, particularly for features that generate pressure waves in directions not aligned with the array.

For situations in which an increase in the angular coverage around the region of interest is not feasible, several hardware- and software-based mitigation strategies have been proposed to date. Hardware-based approaches include the addition of an acoustic reflector to form an additional virtual array to effectively double the detection view [81], synthetic aperture focusing [82], or the use of curved linear array transducers [83]. Computational approaches to mitigate limited view artifacts include specialized modifications to the reconstruction algorithm, such as the inclusion of adaptive weighting for filtered backprojection [84].

8.1.2. Sparse view

A sparse arrangement of detection elements can be necessary for PAI hardware systems, for example, due to budget considerations [70], when attempting to maximize the imaging speed [85], or by attempting to minimize the hardware or computational complexity [86]. Spatial under-sampling also gives rise to grating lobes. There are additional beams created by an array transducer and result from constructive interference caused by periodic spacing of the elements when the element spacing is greater than half the wavelength of the ultrasound wave [87]. Such spatial under-sampling leads to characteristic streaking artifacts, which can be seen both in idealized simulations (Fig. 14**A–D**) but also on *in vivo* images (Fig. 14**E–H**) [85]. In some situations,

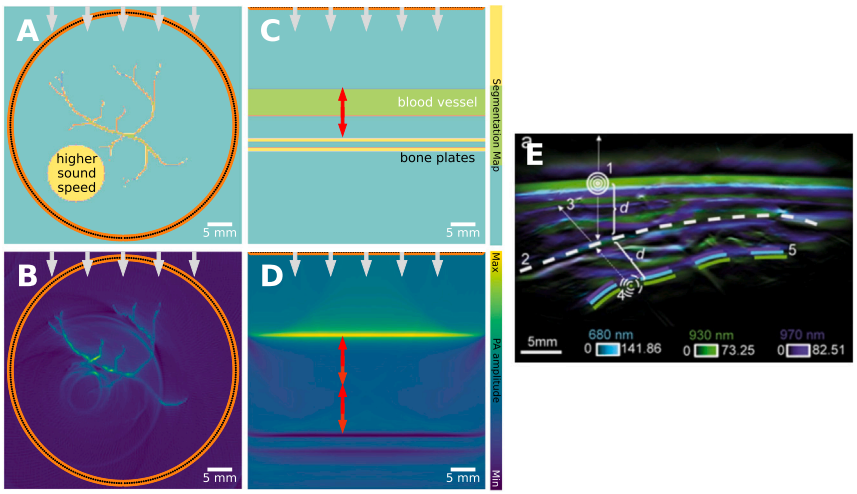

Fig. 10. Acoustic reflections artifact: leads to clutter. **A**: a schematic of a vascular target with a background sound speed of 1540 m/s and a heterogeneity (yellow disc, 1800 m/s). **B**: the image corresponding to **A**, reconstructed assuming a constant sound speed and therefore showing clutter (scattering) artifacts due to the reflections from the region of higher sound speed. **C**: a schematic of a single vessel imaged near a bone. **D**: the image corresponding to **C**, reconstructed assuming a constant sound speed, and the reflections from the bone are clearly visible at twice the blood-bone distance (red arrow). **E**: *in vivo* image [23] of a papillary thyroid carcinoma, delineated in white. The PA image exhibits reflection artifacts (dashed line 5) of the skin signal caused by the capsule of the thyroid nodule (dashed line 2). PA signals originating in point 1 are reflected at the capsule (arrow 3), and an artificial source (point 4) is mirrored to the opposite side. The *in vivo* image is reprinted from Noltes et al. 2023 [23], under a CC BY 4.0 license. The experimental data were captured with a commercially available imaging system (MSOT Acuity Echo, iThera Medical GmbH, Germany).

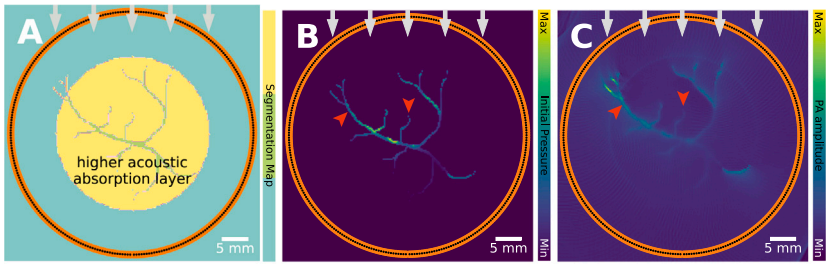

Fig. 11. Acoustic attenuation artifact: leads to signal loss with depth. **A**: Schematic of a vascular network in tissue which is homogeneous except for a region with higher absorption (yellow). **B**: Initial pressure, i.e., before acoustic absorption, **C**: Image reconstructed while there is absorption in the medium (yellow region), but the reconstruction assumes there is none. The waves that have traveled through the most tissue (those traveling from the image center) are most strongly absorbed. As absorption is stronger at higher frequencies, the images are most blurred near the center (compare the two vessels pointed to by the arrowheads, one near the center, one near the edge of the absorbing region).

it can be possible to address the problem through view interpolation, synthetic aperture imaging by mechanically translating a sparse array to effectively increase detector density at the cost of imaging speed, or via the use of a carefully chosen regularization term during iterative reconstruction, such as enforcing a total variation constraint [88].

8.2. Response of the detector elements

There is also a limit to the efficiency with which detection elements can measure the acoustic pressure in a medium. This efficiency depends on three main factors: the incident angle of the wave onto the detection element (referred to as the *detector directivity*), the sampling rate of the detection element (referred to as the *temporal sampling*), and the frequency components of the wave (referred to as the *frequency response*).

8.2.1. Detector directivity

We often assume that detector elements are perfectly omnidirectional, but in reality, detectors are sensitive to the direction of the incoming sound waves. To achieve an omnidirectional response, infinitely small point pressure detectors would be required. Real detectors have a finite aperture size, however, and are most sensitive to sound waves arriving perpendicular to their surface and gradually less sensitive with oblique angles [91]. When ignored in the image reconstruction, the finite aperture size leads to a significant blurring effect in the reconstructed images, where the degree of the blurring increases with the aperture size [92] (Fig. 15).

A high directivity (implemented by a large aperture size) may be beneficial to reduce the influence of out-of-plane contributions, and line detectors with extreme dimensions can even reduce the reconstruction to a Radon transform [93]. However, the image quality can be significantly impacted by a high directivity, with an increased degree of blurring. In practice, we can have a large element size in the elevation direction to give a thin image plane, while having a small element size in-plane, retaining a high resolution [91]. It should also be noted that detector directivity is frequency-dependent.

8.2.2. Limited temporal sampling

The sampling rate of an imaging system inherently limits the maximum detectable frequency as apparent from the Nyquist sampling

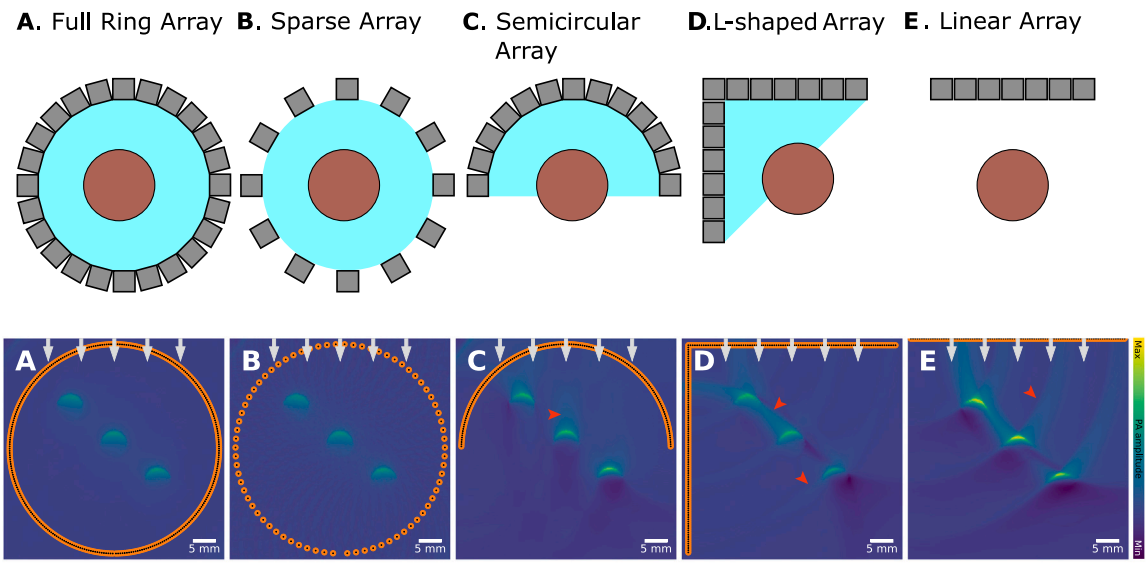

Fig. 12. Example visualization of various typical detector configurations for PAI devices. Three blood vessels are shown and images are reconstructed from simulations of the following detector configurations: **A**: a full-ring array, **B**: a sparse full-ring array, **C**: a semi-circular array, **D**: an L-shaped array, and **E**: a linear array. The upper row shows schematics, including the *visible region* of the image highlighted in light blue, which is described by the envelope of the detection curve (2D) or surface (3D). Since the linear array (shown in **E**) does not enclose any region, no visible region is highlighted in blue. The lower row shows simulations of the same initial pressure distribution but measured and reconstructed with different detection geometries.

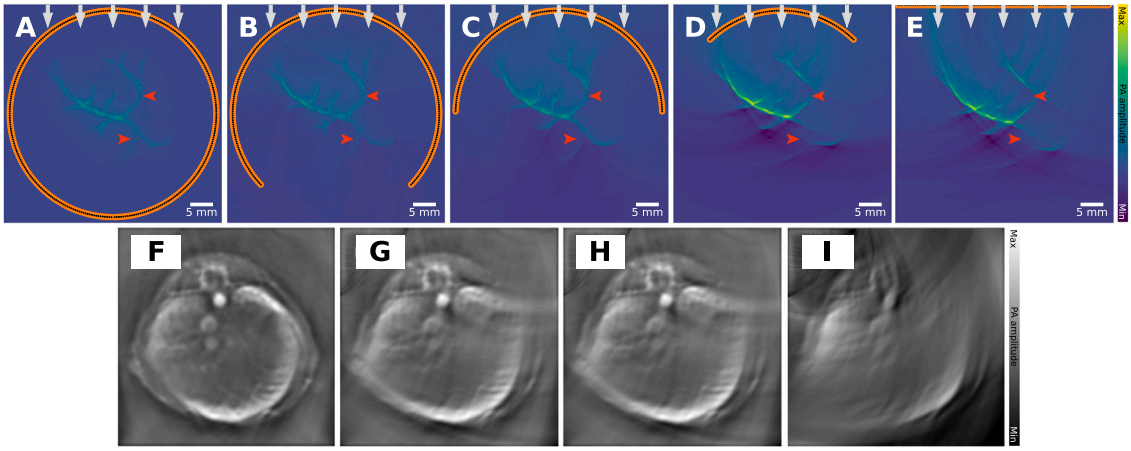

Fig. 13. Limited view artifact: leads to clutter and signal loss. A vascular network is simulated under identical settings, except the detector opening angle of a spherical detector changes. As the detection region (the region that is enclosed by the detectors) becomes smaller (**A**: 360°, **B**: 270°, **C**: 180°, **D**: 90°, **E**: linear transducer) the image quality increasingly drops. We show the limited view artifacts for simulations (**A–E**) as well as preclinical *in vivo* data, in this case of a mouse (**F–I**). **F**: 180°, **G**: 120°, **H**: 90° and **I**: 70°. The *in vivo* images have been reprinted from Xiao et al. 2025 [89], which is available open-access under a CC BY-NC-ND 4.0 license. The experimental data were captured with the TROPUS imaging system, which has a ring detection array and twelve laser bundle outputs distributed in 60° intervals on either side of the ring array [90].

theorem [94]. The theorem states that one has to sample at twice the frequency that should still be detectable. All frequency components above this threshold can lead to undersampling (or aliasing) artifacts. Most conventional ultrasound data acquisition units use a sampling rate of (at least) 40 MHz, which means that the maximum detectable frequency in the signal is limited to 20 MHz. In cases where the sampling rate is below the major frequency components of the acoustic waves, significant aliasing artifacts and blurring can be expected, which can be seen in Fig. 16. In some situations, it can be possible to mitigate these artifacts, for example through the application of a simple frequency-domain filter [95], or through compressive sensing techniques [96].

8.2.3. Limited frequency response

The temporal sampling discussed above introduces a natural upper bound of the detectable frequency components of the acoustic waves. Furthermore, different types of detectors have varying sensitivity to the frequency components of the incoming waves. The relationship of sensitivity and frequency is referred to as the *impulse response* of the system. It describes how the imaging devices react to a sharp rise and fall in sound pressure (an ideal Dirac impulse) as a function of sensitivity over wavelength. In the case of piezoelectric ultrasound transducers, these are typically characterized using a center frequency and a bandwidth. Depending on the impulse response of the imaging

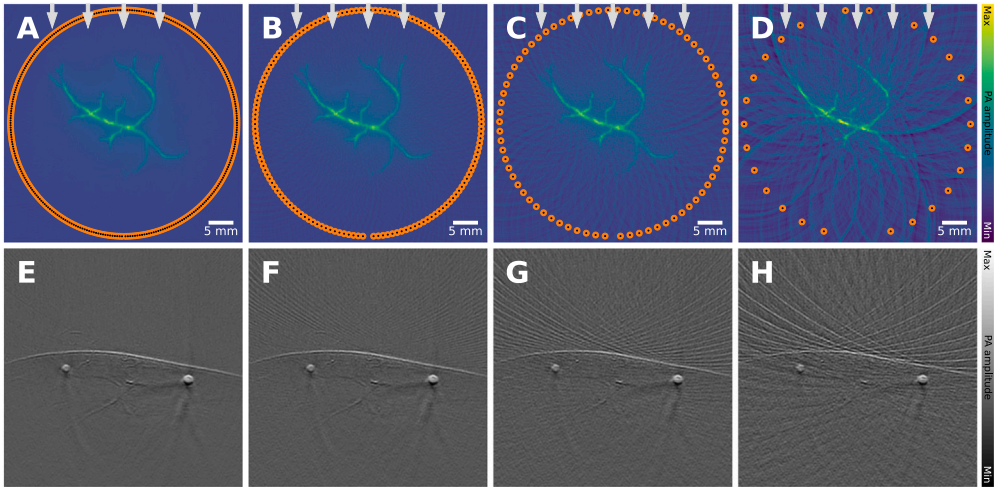

Fig. 14. Sparse view artifact: leads to clutter and signal loss. A vascular network is imaged under identical settings, except for the detector density changes. As the number of detectors becomes smaller (**A**: 298, **B**: 148, **C**: 74, **D**: 28) the image quality increasingly drops. The increase in the characteristic streaking artifact is visible both in the simulations (**A–D**) as well as *in vivo* images (**E–H**). The *in vivo* images show a human forearm imaged with a semicircle array (radius: 40 mm and 180° opening angle), **E**: 256, **F**: 128, **G**: 64 and **H**: 32 elements. **E–H** have been reprinted from Ozdemir et al. 2022 [85], which is available open-access under a CC BY 4.0 license. The experimental data were captured with a custom semi-circular transducer array combined with a pulsed laser.

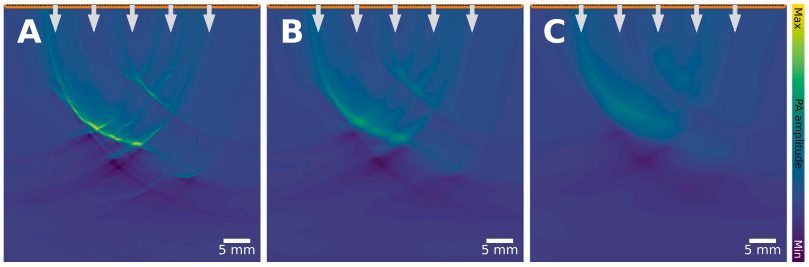

Fig. 15. Detector directivity artifact: leads to blurring. A vessel tree is simulated with a linear array featuring three aperture sizes, increasing in size from **A** (detector element width of 0.24 mm) to **C** (detector element width of 5 mm).

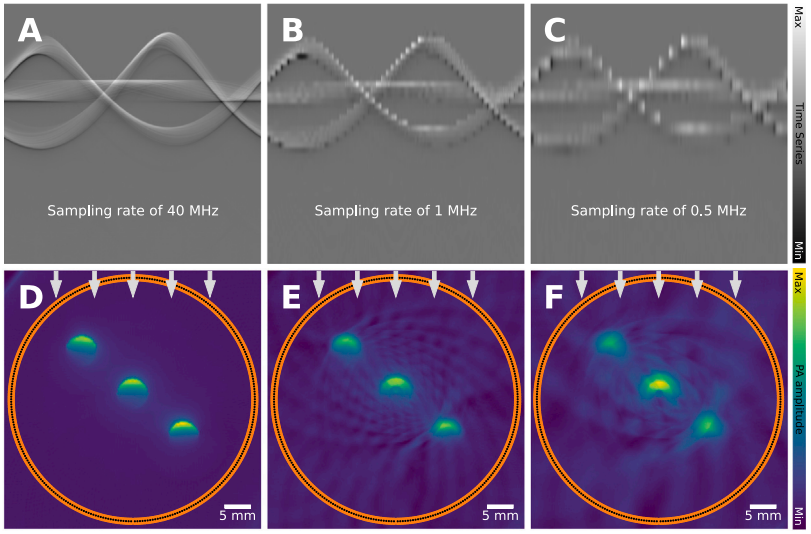

Fig. 16. Limited temporal sampling artifact: leads to blurring, clutter and signal loss. 3 blood vessels are imaged under identical settings, except the temporal sampling rate changes. As the Nyquist sampling theorem is increasingly violated (**A**: 40 MHz, **B**: 1 MHz, **C**: 0.5 MHz), artifacts occur.

system, measurements of the same sound waves can drastically vary, which can be seen in Fig. 17.

Capturing high-frequency components of the ultrasound wave is important to reconstruct a sharp image, but noise also manifests significantly in the higher frequencies. To mitigate this, low-pass filters are often applied prior to image reconstruction, which can mitigate noise but have to be traded off with a potential blurring of the image. Conversely, if the impulse response function limits the capture of lower frequencies, information can be lost from smoothly varying or piecewise-constant regions. Several mitigation strategies have

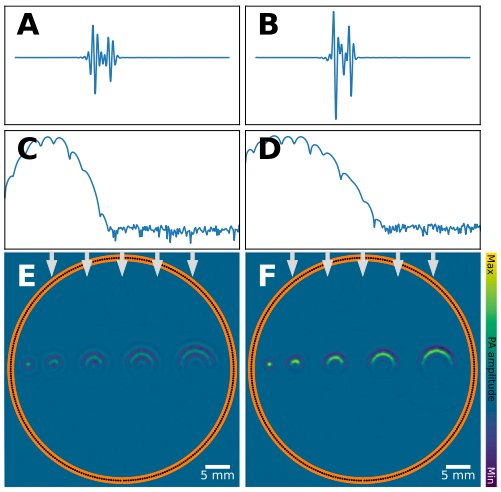

Fig. 17. Limited frequency response artifact: leads to blurring, clutter and signal loss. 5 tubes with increasing diameter (from 1 mm to 6.6 mm) are imaged under identical settings, except the detector bandwidth changes. Transducers have a limited bandwidth, here modeled as a frequency domain Gaussian filter with a certain bandwidth and a center frequency. **A**: 1 MHz, 0.5 MHz, **B**: 1 MHz, 0.8 MHz: center frequency and bandwidth respectively. We show the time series data trace for one detection element (**A&B**), the frequency content of the measured signals (**C&D**), and the reconstructed tubes (**E&F**). One can clearly see differences in the signal amplitudes and the sharpness of the reconstructed tubes.

been proposed for the loss of low frequencies, including deconvolution with [97,98] or without [99] known impulse response, or by using deep learning-based data priors for correction [100,101].

8.3. Measurement noise

Stochastic changes to the measurements can arise from several sources, including thermal and electrical effects [102]. The amount of noise in an image is often quantified using specific measures, such as the signal-to-noise ratio (SNR), the contrast-to-noise ratio (CNR) [103], or the generalized contrast-to-noise ratio (gCNR) [104]. For all of these measures, the relative signal differences in two regions of interest (one corresponding to noise, and one to the target signal) are analyzed. Common mitigation strategies include the use of data filtering techniques [105] or by using dimensionality reduction techniques to separate meaningful signal from noise [106,107]. However, as with other artifacts introduced in this review, measurement noise may not always be clearly differentiable from real signals, see Fig. 18. For example, if the distribution of signals is high-frequency, a reconstructed image of high Gaussian noise might look qualitatively comparable. Additionally, detectors have a noise floor, referred to as the *noise-equivalent pressure* [102], which quantifies the minimum acoustic pressure fluctuations that are measurable.

9. Artifact source: Patient

Properties of human subjects, such as the presence of highly optically absorbing structures like melanin in the epidermis, or structures with very different acoustic properties, such as bone and soft tissue underlie many of the artifacts already introduced. Additionally, however, human imaging poses unique challenges that do not fall under any of the previous categories.

9.1. Patient movement

Patient movement poses a substantial challenge for accurate and high-quality clinical PAI. Motion artifacts depend closely on the imaging speed, so systems with low laser pulse repetition rates or slow ultrasound acquisition rates are particularly affected by this. Furthermore, certain anatomical sites are more susceptible to motion artifacts because of breathing and heartbeat-induced motion, for example, near the lungs in breast imaging, or melanoma imaging of the torso or back [108]. Mitigation strategies are therefore crucial to enable reliable clinical imaging of these organs.

The effects of patient motion on PAI depends on the exact image acquisition procedure, such as the resolution, frame rate and post-processing procedure. In a system with a fixed array of transducers, such as typical tomographic clinical systems, each frame is acquired in less than 50 μs, as determined by the sound speed and field of view. Therefore, for any substantial artifact to be induced over the course of a single frame, motion greater than the resolution limit would have to occur on that time frame. For a typical resolution of 100 μs, this would require motion faster than around 2 m/s, which is much faster than even blood flow in arteries (~ 0.3 m/s [109]), so no significant artifact is expected in a single-shot frame. Multi-wavelength imaging, or averaging across multiple frames, however, occurs on a much slower time scale (~ 10 Hz for tuneable laser systems), where motion between wavelengths is certainly possible, see Fig. 19. Motion due to probe movement by the operator or breathing motion could lead to features like blood vessels appearing in different locations depending on wavelength and split or blurred in the case of frame averaging. If spectral unmixing is then applied to resolve the contributions of different biomolecules to the photoacoustic spectrum, the motion of the patient means that the spatial location of a given pixel will have changed during the scan, rendering spectral unmixing results meaningless.

Several strategies exist to mitigate the influence of motion on PA data. One straightforward approach is breath-hold imaging, which minimizes motion-related distortions in thoracic and abdominal imaging by instructing the subject to hold their breath during data acquisition [108] (Fig. 19**C**). However, this is not always feasible, especially in clinical settings involving long imaging times. Computational methods offer alternative solutions, such as the approach demonstrated by Schwarz et al. [110] in Raster-Scan Optoacoustic Mesoscopy (RSOM, iThera Medical GmbH, Germany), where motion correction is achieved by identifying the position of the melanin layer in the skin and using it to correct the wavefront distortions. Another method involves selective frame averaging [111], where adjacent frames are compared based on an image quality metric, and averaging is only applied when images meet a predefined similarity threshold. This technique helps reduce motion blur without introducing excessive loss of spatial resolution. Additionally, optical flow-based correction has been proposed to track motion across frames by computing a deformation map. However, this method faces challenges in multi-wavelength imaging, where spectral variations alter image features. A possible solution is to compute the optical flow map on a co-registered ultrasound image, then apply the derived deformation map to the PA scan, thus improving the robustness of motion correction across different wavelengths [112].

9.2. Patient preparation

Lack of correct preparation of the patient can result in artifacts, as shown in Fig. 20. For example, hair on the surface of the skin can strongly absorb light, particularly in darker hair types [113]. Due to the limited-view artifacts induced in practical clinical PAI systems, absorption in the skin surface will lead to artifacts below the skin surface (Fig. 20**B&E**). This could qualitatively and quantitatively affect the image below the skin surface, by introducing extraneous signal, or reducing the contrast between the background, non-absorbing tissue and the target of interest. To mitigate this source of artifacts, a suitable hair-removal protocol should be followed, by shaving, waxing, or using depilatory cream on the imaging site.

Air bubbles (which can be present in, e.g., coupling gel) lead to large spatial differences in the sound speed and density. The differences

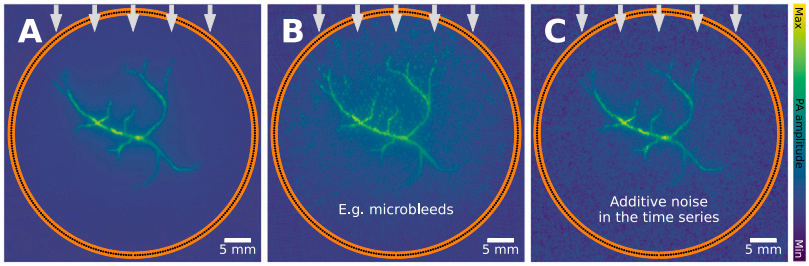

Fig. 18. Measurement noise artifact: leads to signal loss at low SNR, and clutter. A vascular network is imaged under identical settings, except noise is introduced in **B** and **C**. **B**: small clusters of blood are introduced (e.g., due to microbleeds), **C**: noise (zero-mean additive Gaussian noise, with a standard deviation of 0.05) is added to the time series. Both result in a similar reconstructed image, which can complicate image analysis.

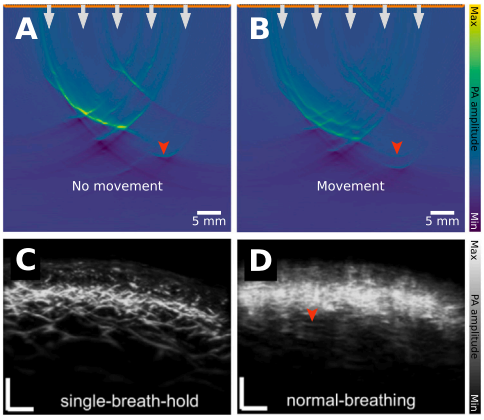

Fig. 19. Patient movement artifact: leads to clutter and blurring. Measurements are often repeated, e.g., to average and reduce random noise. The assumption is that the patient is stable and does not move. **A**: the assumption holds, where 3 (identical) time series of the vascular network are recorded and averaged. **B**: there is movement between frames, and the 3 time series differ, resulting in decreased image quality. This can also be seen in **in vivo** data (**C&D**), where the skin on the back of a healthy volunteer is imaged. **C**: acquired while the breath was held for 15 s (single-breath-hold), and **D**: acquired during normal breathing. The *in vivo* images have been reprinted from He et al. 2022 [114], which is available open-access under a CC BY 4.0 license. The experimental data were captured with a raster-scanned single transducer element with a single laser fiber delivering the light through the center aperture.

in acoustic properties between biological tissue and the air bubbles lead to acoustic reflections, violating the assumption of straight-line unimpeded acoustic propagation made in the image reconstruction. Violation of these image reconstruction assumptions means that the image is blurred, the signal intensity is reduced, and sometimes regions of very low or negative signal intensity can be seen (Fig. 20**C&F**). Similar artifacts may be observed when imaging gas-filled structures in the body, such as the intestines, as highlighted in images of phantom materials without proper degassing of the material [115].

10. Advanced mitigation strategies

A plethora of PA image reconstruction algorithms have been proposed to recover initial pressure distributions from PA time series measurements. We do not attempt a comprehensive review here of a substantial body of work, but note in passing that the various approaches include one-step filtered backprojection-type methods [116, 117], beamforming [118–120], time reversal [121–123], iterative reconstruction schemes [124–126], optimization approaches using numerical models of acoustic propagation [96,127,128], and more recently deep learning-based reconstruction schemes [129–131]. The important point is that all these reconstruction methods incorporate a model approximating the physics of the acoustic propagation and detection. While this model may not always be explicitly stated, it is inherently present. Inaccuracies in the physics model are one of the two fundamental reasons why artifacts occur in images; the other being insufficient data. Corresponding to these two fundamental causes of the artifacts are two corresponding classes of approaches to mitigating artifact generation, which we describe in the next sections, as well as deep learning and deconvolution-based approaches.

10.1. Improving the model

If the artifacts are due to inaccurate approximations in the physical model, improving the physical model may remove them. For example, the approximation that the sound speed has no spatial variation is not always true and the resulting artifacts can be ameliorated by incorporating a more accurate representation of the sound speed in the model used in the reconstruction. There are two challenges to this: knowing what the correct physical model should be (in this example, knowing the correct sound speed map), and incorporating it into the reconstruction algorithm. Two-sound speed models have been used to reduce blurring when the coupling medium has a different sound speed from the tissue and the two regions and their average sound speeds are known a priori, or the regions can be segmented from a preliminary image and literature values used for the sound speeds [132,133]. However, in more general cases, the sound speed distribution must be estimated using ultrasound tomography [61,134–137]. Once a model of the sound speed distribution has been obtained, by whatever means, the challenge is to incorporate it into the PA reconstruction. In the two-sound speed case, backprojection methods can be readily adapted. Models that can account for more general sound speed maps include series-based approaches [124–126] or iterative image reconstruction approaches based on the minimization of a functional (an objective, cost or loss function) that measures the closeness of fit of a numerical model to the data [96,127,138,139]. In this latter case, the main challenges become keeping the computational burden manageable and accelerating the convergence of the minimization. For small data sets and image sizes, it is possible to form the required operators explicitly in matrix form and exploit recent advances in linear algebra but these tasks become non-trivial for large 3D images and data sets. Sound speed estimation from the PA images or PA data itself has been proposed, but, while interesting, it is still under investigation [140–144].

10.2. Supplementing the data

If the artifacts are due to insufficient data, the ideal solution is to record more data, but that is not always possible. However, sometimes the artifacts can be removed by restricting the class of possible images during the image reconstruction stage by incorporating additional information, e.g., prior knowledge of the object, such as that it must be non-negative, or piecewise constant, or take a certain form. Some prior information can be used in a post-processing step, e.g., by using a vessel filter [145] when the image is known to contain vessels, or applying a non-negativity condition when the physical principles dictate that it must be the case. Priors may also be obtained from adjunct imaging

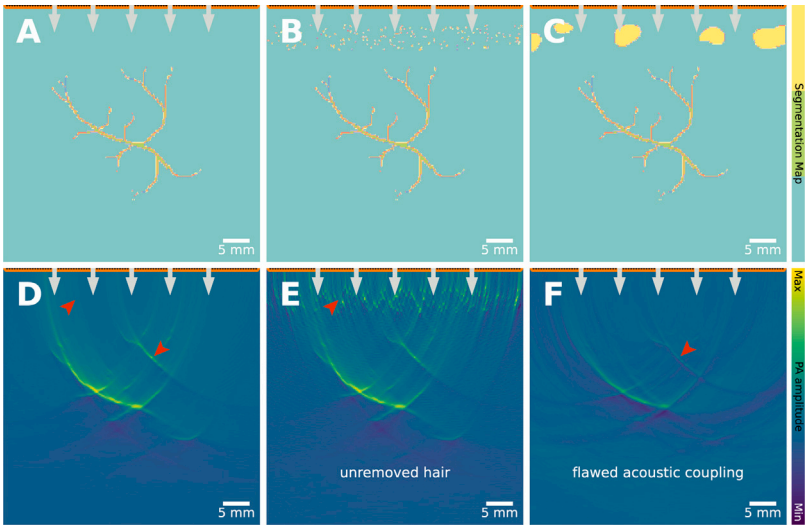

Fig. 20. Patient preparation artifact: leads to clutter. A vascular network is imaged under identical settings, except for changes in quality of patient preparation. **B**: shows hairs that should have been removed before measurement, resulting in strong absorption and decreased image qualify when compared to the ideal case in **A**. **C**: shows air bubbles between transducer and object, which strongly distort the time series and the resultant image.

modalities, often ultrasound imaging [146–148]. However, functional-minimization image reconstruction approaches, mentioned above, offer a more systematic approach as additional terms, *penalty* terms, can be added to the functional to promote images of a certain type. The total variation approach, which promotes piecewise constant solutions, is commonly implemented in this way. A related approach will ensure an image satisfies a prior by iterating between updating an image estimate based on the data and projecting that image into the space of allowed solutions using a proximal operator [88,96,127,149–152].

10.3. Deep learning

Because model-based functional minimization methods for image reconstruction can be computationally intensive, deep learning networks, which are slow to train but fast to run, have been proposed as a means of speeding up reconstruction times. Furthermore, learned components can be used at every step of the image reconstruction pipeline: to preprocess the data, e.g., to remove noise, to generate the initial guess of an iterative reconstruction, to act as a model of the physics, to learn a prior to compute an image update, to post-process the image, e.g., to remove artifacts, and even to replace the whole image reconstruction pipeline with a learned end-to-end data-to-image reconstruction. The use of deep learning in medical image reconstruction in general, as well as in photoacoustics, is a fast-changing field. We will therefore not include references here, other than to point the interested reader to some review articles [153–159]. As this is a paper on artifacts, it must be noted that any learned method is only as good as the data used to train it, and that over-reliance on the learned distribution in preference to the measured data can result in *hallucinations*: artifacts generated by the learned component and not arising from the data.

10.4. Deconvolution

Deconvolution is widely used in data space as a method for correcting for the frequency response of acoustic response of the detector elements [160], as well as in image space to correct for the point-spread function (PSF) of the PAI system [161]. Deconvolution is essentially a re-weighting of the frequency components of a signal (or spatial frequency components of an image) to account for the non-ideal response of the detector or imaging system. This can be beneficial, as attenuated frequency components can be restored to their correct amplitude. However, care must be taken. First, when a frequency component has been attenuated to the extent that is it indistinguishable from the noise, or when it has simply not been measured because of the limitations of the system, naive deconvolution will amplify the noise, corrupting the image. Regularization of the deconvolution is therefore necessary. Second, when deconvolving an image PSF from an image, it is often assumed that the PSF is spatially invariant. This allows the deconvolution to be applied efficiently using Fast Fourier Transforms. However, this assumption of spatial invariance will not always hold, for instance, limited-view artifacts are not usually spatially invariant. Note that image reconstruction schemes in which the model of the detection system (e.g., the frequency- and directional-dependence of the detector elements) is included in the model of the physics used in the reconstruction, will effectively, implicitly, deconvolve the PSF from the image during the image reconstruction process.

11. Discussion

As photoacoustic imaging makes its way from the laboratory to the clinic, the presence of artifacts could adversely affect patient care if not identified or corrected. Here, we have presented an overview of the mechanisms responsible for artifact generation and illustrated them, providing a taxonomy and example images. This can serve as a guide for clinical users, but also developers of novel PA systems.

Artifacts in PAI have substantial implications for its clinical use, where we hope that our work can be of use for furthering the understanding and mitigation options for commonly encountered artifacts. For example, one of the FDA-approved PAI systems calculates oxygenation maps, which can be used as a biomarker in tumor diagnosis [162]. Various light-tissue interaction artifacts can distort this oxygenation map, such as spectral coloring and out-of-plane absorption. The distortion of the oxygenation map can, in turn, lead to a misdiagnosis of the tumor if clinical users are not familiar with this inherent limitation. Moreover, as the sound speed varies substantially in human tissue, from 1450 m/s for fat to 4080 m/s for bone [163], and also between pathology [164], sound speed artifacts are likely to occur in PAI. These artifacts will hamper the investigation of the size, shape, and characteristics of structures, which could mean incorrect risk stratification [165]. In contrast, artifacts may also carry diagnostic information. For example, in ultrasound, the so-called comet-tail artifact can be used for finding gallstones [166], and in CT the blooming artifacts can highlight calcifications [167]. Our overview of artifacts in PAI

can therefore help with preventing confounding during the diagnostic process, but also assist in the diagnostic process.

By listing the limitations of current PAI systems and demonstrating the origins of the resulting artifacts, we hope that this work will assist those working to improve PAI in the future. Previously, in-depth knowledge of the out-of-plane absorption artifact allowed for the formulation of a transducer displacement method for reducing their influence [168]. As mentioned, sound speed artifacts have also been ameliorated by integrating ultrasound tomography into photoacoustic systems, such that the measured sound speed maps can be used during the reconstruction [169]. Recently, deep learning methods have also been introduced in combination with PAI, either as post-processing correction algorithms [130] or by directly learning the reconstruction [70], but (artifact) hallucinations may hamper their usefulness. Physics-driven deep learning, where one embeds knowledge of physical laws, has shown high-quality results in PAI [170].

While we have discussed many artifacts, the scope of this paper is limited to artifacts that originate outside of the reconstruction step. There are different reconstruction algorithms for PAI, each with their own advantages and disadvantages [171]. While a reconstruction algorithm may dampen the impact of certain artifacts, it can also increase the impact of others or even introduce new artifacts. These reconstruction artifacts are often characteristic of the chosen algorithm, as they handle data limitations differently. For example, some algorithms may result in negative values in the reconstructed image [172], backprojection has shown to result in more pronounced streak artifacts [173], and deep learning techniques could induce artifacts by hallucination. In this work, we did not systematically investigate the influence of the choice of reconstruction algorithm on the reconstructed image quality, though that would undoubtedly be of great interest to the PAI community.

In addition to differences in reconstruction algorithms, there also exist many *ad-hoc* pre- and postprocessing schemes that are widely used. Such computational steps usually significantly change the image content and alter how the data is perceived by the user. For example, the application of vesselness filters (such as the Frangi vesselness filter [145]) is quite common in PAI [174], however, such an approach can provide inconsistent and possibly misleading results when applied to PA images obtained under realistic conditions [175]. Other approaches include the application of a variety of false-color scales, which can non-linearly affect the contrast of image features. These are just two common examples, but all of these methods come hand-in-hand with their own characteristic shortcomings that a user of the technology needs to keep in mind when, for example, basing clinical decisions on the images.

12. Summary

An idealized photoacoustic system would provide an image that corresponds spatially and spectrally to the morphological and molecular properties of the tissue. However, modeling assumptions must often be made in image reconstruction and post-processing to ensure computational tractability, leading to artifacts where the assumptions break down. Furthermore, clinical requirements, physics constraints and practical limitations can mean that incomplete data is provided. As the image reconstruction algorithms place several requirements on the amount of data collected, these incomplete datasets will lead to artifacts. Artifacts can be mitigated with certain strategies, such as other reconstruction models, more complete datasets, and including prior knowledge in the reconstruction, but currently, artifacts cannot be prevented entirely. Artifacts have the potential to adversely affect results by introducing false features or obscuring true features, significantly hampering the clinical translation of PAI. We believe that an in-depth awareness and knowledge of the origins of PA artifacts is a critical step to catalyze future innovations for the development of mitigation strategies.

CRediT authorship contribution statement

Max T. Rietberg: Conceptualization, Software, Writing – review & editing, Writing – original draft. **Janek Gröhl:** Conceptualization, Writing – original draft, Writing – review & editing. **Thomas R. Else:** Writing – original draft, Writing – review & editing, Conceptualization. **Sarah E. Bohndiek:** Writing – review & editing, Writing – original draft, Conceptualization. **Srirang Manohar:** Conceptualization, Writing – review & editing, Writing – original draft. **Benjamin T. Cox:** Conceptualization, Writing – original draft, Writing – review & editing.

Declaration of competing interest

The authors declare that they have no known competing financial interests or personal relationships that could have appeared to influence the work reported in this paper.

Acknowledgments

MTR and SM acknowledge the funding from KWF, TKI-Life Sciences and Health and Seno Medical Instruments in project THYNAS+ (2023-PPS/15564). MTR and SM acknowledge the Top Technology Twente Connecting Industry program with Seno Medical Instruments in project PeTRUS. SM acknowledges funding from EFRO-Oost project 00103 Elastografie voor snellere herkenning van borstkanker in 3D fotoakoestieche mammografie. The work of JG was supported by the Deutsche Forschungsgemeinschaft, Germany (DFG, German Research Foundation) under projects GR 5824/1 and GR 5824/2. SEB and TRE were supported by Cancer Research UK, United Kingdom under grant number C9545/A29580 and the UKRI Engineering and Physical Sciences Research Council under grant numbers EP/X037770/1, EP/R003599/1 and EP/V027061/1. BTC acknowledges support from the Engineering and Physical Sciences Research Council, UK (EPSRC), grants EP/W029324/1, EP/T014369/1.

Appendix A. Supplementary data

Supplementary material related to this article can be found online at https://doi.org/10.1016/j.pacs.2025.100745.

Data availability

Code will be published: https://gitlab.com/MTRietberg/artifact-paper.

References

[1] P. Suetens, Fundamentals of Medical Imaging, Cambridge University Press, 2017.
[2] W. Sureshbabu, O. Mawlawi, PET/CT imaging artifacts, J. Nucl. Med. Technol. 33 (3) (2005) 156–161.
[3] E.M. Bellon, E.M. Haacke, P.E. Coleman, D.C. Sacco, D.A. Steiger, R.E. Gangarosa, MR artifacts: a review, Am. J. Roentgenol. 147 (6) (1986) 1271–1281.
[4] D.A. Boas, D.H. Brooks, E.L. Miller, C.A. DiMarzio, M. Kilmer, R.J. Gaudette, Q. Zhang, Imaging the body with diffuse optical tomography, IEEE Signal Process. Mag. 18 (6) (2001) 57–75.
[5] L.V. Wang, H.-i. Wu, Biomedical Optics: Principles and Imaging, John Wiley & Sons, 2007.
[6] L.V. Wang, S. Hu, Photoacoustic tomography: in vivo imaging from organelles to organs, Science 335 (6075) (2012) 1458–1462.
[7] T. Chen, L. Liu, X. Ma, Y. Zhang, H. Liu, R. Zheng, J. Ren, H. Zhou, Y. Ren, R. Gao, et al., Dedicated photoacoustic imaging instrument for human periphery blood vessels: a new paradigm for understanding the vascular health, IEEE Trans. Biomed. Eng. 69 (3) (2021) 1093–1100.
[8] E.L. Brown, T.L. Lefebvre, P.W. Sweeney, B.J. Stolz, J. Gröhl, L. Hacker, Z. Huang, D.-L. Couturier, H.A. Harrington, H.M. Byrne, et al., Quantification of vascular networks in photoacoustic mesoscopy, Photoacoustics 26 (2022) 100357.

[9] A.B.E. Attia, G. Balasundaram, M. Moothanchery, U. Dinish, R. Bi, V. Ntziachristos, M. Olivo, A review of clinical photoacoustic imaging: Current and future trends, Photoacoustics 16 (2019) 100144.

[10] J. Jo, G. Xu, M. Cao, A. Marquardt, S. Francis, G. Gandikota, X. Wang, A functional study of human inflammatory arthritis using photoacoustic imaging, Sci. Rep. 7 (1) (2017) 15026.

[11] F. Knieling, C. Neufert, A. Hartmann, J. Claussen, A. Urich, C. Egger, M. Vetter, S. Fischer, L. Pfeifer, A. Hagel, et al., Multispectral optoacoustic tomography for assessment of Crohn's disease activity, N. Engl. J. Med. 376 (13) (2017) 1292–1294.

[12] A.P. Regensburger, E. Brown, G. Krönke, M.J. Waldner, F. Knieling, Optoacoustic imaging in inflammation, Biomedicines 9 (5) (2021) 483.

[13] M. Li, Y. Tang, J. Yao, Photoacoustic tomography of blood oxygenation: a mini review, Photoacoustics 10 (2018) 65–73.

[14] J. Gröhl, T. Kirchner, T.J. Adler, L. Hacker, N. Holzwarth, A. Hernández-Aguilera, M.A. Herrera, E. Santos, S.E. Bohndiek, L. Maier-Hein, Learned spectral decoloring enables photoacoustic oximetry, Sci. Rep. 11 (1) (2021) 6565.

[15] W.C. Vogt, X. Zhou, R. Andriani, K.A. Wear, T.J. Pfefer, B.S. Garra, Photoacoustic oximetry imaging performance evaluation using dynamic blood flow phantoms with tunable oxygen saturation, Biomed. Opt. Express 10 (2) (2019) 449–464.

[16] V. Ntziachristos, D. Razansky, Molecular imaging by means of multispectral optoacoustic tomography (MSOT), Chem. Rev. 110 (5) (2010) 2783–2794.

[17] J. Yao, L.V. Wang, Recent progress in photoacoustic molecular imaging, Curr. Opin. Chem. Biol. 45 (2018) 104–112.

[18] J. Weber, P.C. Beard, S.E. Bohndiek, Contrast agents for molecular photoacoustic imaging, Nature Methods 13 (8) (2016) 639–650.

[19] Q. Fu, R. Zhu, J. Song, H. Yang, X. Chen, Photoacoustic imaging: contrast agents and their biomedical applications, Adv. Mater. 31 (6) (2019) 1805875.

[20] L. Lin, L.V. Wang, The emerging role of photoacoustic imaging in clinical oncology, Nat. Rev. Clin. Oncol. 19 (6) (2022) 365–384.

[21] A. Karlas, M.A. Pleitez, J. Aguirre, V. Ntziachristos, Optoacoustic imaging in endocrinology and metabolism, Nat. Rev. Endocrinol. 17 (6) (2021) 323–335.

[22] A. Oraevsky, B. Clingman, J. Zalev, A. Stavros, W. Yang, J. Parikh, Clinical optoacoustic imaging combined with ultrasound for coregistered functional and anatomical mapping of breast tumors, Photoacoustics 12 (2018) 30–45.

[23] M.E. Noltes, M. Bader, M.J. Metman, J. Vonk, P.J. Steinkamp, J. Kukačka, H.E. Westerlaan, R.A. Dierckx, B.M. van Hemel, A.H. Brouwers, et al., Towards in vivo characterization of thyroid nodules suspicious for malignancy using multispectral optoacoustic tomography, Eur. J. Nucl. Med. Mol. Imaging 50 (9) (2023) 2736–2750.

[24] J.L. Sandell, T.C. Zhu, A review of in-vivo optical properties of human tissues and its impact on PDT, J. Biophotonics 4 (11–12) (2011) 773–787.

[25] J. Gröhl, K.K. Dreher, M. Schellenberg, T. Rix, N. Holzwarth, P. Vieten, L. Ayala, S.E. Bohndiek, A. Seitel, L. Maier-Hein, SIMPA: an open-source toolkit for simulation and image processing for photonics and acoustics, J. Biomed. Opt. 27 (8) (2022) 083010.

[26] T. Kirchner, F. Sattler, J. Gröhl, L. Maier-Hein, Signed real-time delay multiply and sum beamforming for multispectral photoacoustic imaging, J. Imaging 4 (10) (2018) http://dx.doi.org/10.3390/jimaging4100121, URL https://www.mdpi.com/2313-433X/4/10/121.

[27] B.T. Cox, B.E. Treeby, Artifact trapping during time reversal photoacoustic imaging for acoustically heterogeneous media, IEEE Trans. Med. Imaging 29 (2) (2009) 387–396.

[28] W.C. Vogt, X. Zhou, R. Andriani, K.A. Wear, T.J. Pfefer, B.S. Garra, Photoacoustic oximetry imaging performance evaluation using dynamic blood flow phantoms with tunable oxygen saturation, Biomed. Opt. Express 10 (2) (2019) 449–464, http://dx.doi.org/10.1364/BOE.10.000449, URL https://opg.optica.org/boe/abstract.cfm?URI=boe-10-2-449.

[29] T. Tarvainen, B. Cox, Quantitative photoacoustic tomography: modeling and inverse problems, J. Biomed. Opt. 29 (S1) (2024) S11509.

[30] J. Gröhl, K. Yeung, K. Gu, T.R. Else, M. Golinska, E.V. Bunce, L. Hacker, S.E. Bohndiek, Distribution-informed and wavelength-flexible data-driven photoacoustic oximetry, J. Biomed. Opt. 29 (S3) (2024) S33303.

[31] H. Kruit, K. Joseph Francis, E. Rascevska, S. Manohar, Annular fiber probe for interstitial illumination in photoacoustic guidance of radiofrequency ablation, Sensors 21 (13) (2021) http://dx.doi.org/10.3390/s21134458, URL https://www.mdpi.com/1424-8220/21/13/4458.

[32] T. Mitcham, K. Dextraze, H. Taghavi, M. Melancon, R. Bouchard, Photoacoustic imaging driven by an interstitial irradiation source, Photoacoustics 3 (2) (2015) 45–54, http://dx.doi.org/10.1016/j.pacs.2015.02.002, URL https://www.sciencedirect.com/science/article/pii/S2213597915000051.

[33] H. Guo, Y. Li, W. Qi, L. Xi, Photoacoustic endoscopy: A progress review, J. Biophotonics 13 (12) (2020) e202000217.

[34] M.R. Tomaszewski, M. Gehrung, J. Joseph, I. Quiros-Gonzalez, J.A. Disselhorst, S.E. Bohndiek, Oxygen-enhanced and dynamic contrast-enhanced optoacoustic tomography provide surrogate biomarkers of tumor vascular function, hypoxia, and necrosis, Cancer Res. 78 (20) (2018) 5980–5991.

[35] T. Kirchner, J. Gröhl, L. Maier-Hein, Context encoding enables machine learning-based quantitative photoacoustics, J. Biomed. Opt. 23 (5) (2018) 056008.

[36] M. Dantuma, F. Lucka, S.C. Kruitwagen, A. Javaherian, L. Alink, R.P.P. van Meerdervoort, M. Nanninga, T.J.P.M.O. 't Root, B.D. Santi, J. Budisky, G. Bordovsky, E. Coffy, M. Wilm, T. Kasponas, S.H. Aarnink, L.F. de Geus-Oei, F. Brochin, T. Martinez, A. Michailovas, W.M. Kobold, J. Jaros, J. Veltman, B. Cox, S. Manohar, Fully three-dimensional sound speed-corrected multi-wavelength photoacoustic breast tomography, 2023, arXiv:2308.06754.

[37] H.N.Y. Nguyen, W. Steenbergen, Three-dimensional view of out-of-plane artifacts in photoacoustic imaging using a laser-integrated linear-transducer-array probe, Photoacoustics 19 (2020) 100176, http://dx.doi.org/10.1016/j.pacs.2020.100176, URL https://www.sciencedirect.com/science/article/pii/S2213597920300161.

[38] S.A. Akhmanov, V.A. Vysloukh, A.S. Chirkin, Y. Atanov, Optics of Femtosecond Laser Pulses, Springer, 1992.

[39] c. Özsoy, A. Cossettini, A. Özbek, S. Vostrikov, P. Hager, X.L. Deán-Ben, L. Benini, D. Razansky, LightSpeed: A compact, high-speed optical-link-based 3D optoacoustic imager, IEEE Trans. Med. Imaging 40 (8) (2021) 2023–2029, http://dx.doi.org/10.1109/TMI.2021.3070833.

[40] X. Liu, S.K. Kalva, B. Lafci, D. Nozdriukhin, X.L. Deán-Ben, D. Razansky, Full-view LED-based optoacoustic tomography, Photoacoustics 31 (2023) 100521, http://dx.doi.org/10.1016/j.pacs.2023.100521.

[41] N.A. Rejesh, H. Pullagurla, M. Pramanik, Deconvolution-based deblurring of reconstructed images in photoacoustic/thermoacoustic tomography, J. Opt. Soc. Amer. A 30 (10) (2013) 1994–2001, http://dx.doi.org/10.1364/JOSAA.30.001994, URL https://opg.optica.org/josaa/abstract.cfm?URI=josaa-30-10-1994.

[42] T.J. Allen, P.C. Beard, Pulsed near-infrared laser diode excitation system for biomedical photoacoustic imaging, Opt. Lett. 31 (23) (2006) 3462–3464, http://dx.doi.org/10.1364/OL.31.003462, URL https://opg.optica.org/ol/abstract.cfm?URI=ol-31-23-3462.

[43] M.W. Sigrist, Laser generation of acoustic waves in liquids and gases, J. Appl. Phys. 60 (7) (1986) R83–R122.

[44] G. Diot, S. Metz, A. Noske, E. Liapis, B. Schroeder, S.V. Ovsepian, R. Meier, E. Rummeny, V. Ntziachristos, Multispectral optoacoustic tomography (MSOT) of human breast cancer, Clin. Cancer Res. 23 (22) (2017) 6912–6922.

[45] K. Daoudi, P. Van Es, S. Manohar, W. Steenbergen, Two-dimensional spatiotemporal monitoring of temperature in photothermal therapy using hybrid photoacoustic–ultrasound transmission tomography, J. Biomed. Opt. 18 (11) (2013) 116009.

[46] H. Assi, C. Yang, E. Shaswary, M. Tam, J. Tavakkoli, M. Kolios, G. Peyman, C. Kumaradas, Real-time control of nanoparticle-mediated thermal therapy using photoacoustic imaging, IEEE Trans. Biomed. Eng. 68 (7) (2020) 2188–2194.

[47] J. Kim, W. Choi, E.-Y. Park, Y. Kang, K.J. Lee, H.H. Kim, W.J. Kim, C. Kim, Real-time photoacoustic thermometry combined with clinical ultrasound imaging and high-intensity focused ultrasound, IEEE Trans. Biomed. Eng. 66 (12) (2019) 3330–3338.

[48] E.V. Petrova, H.P. Brecht, M. Motamedi, A.A. Oraevsky, S.A. Ermilov, In vivo optoacoustic temperature imaging for image-guided cryotherapy of prostate cancer, Phys. Med. Biol. 63 (6) (2018) 064002.

[49] Y. Zhou, M. Li, W. Liu, G. Sankin, J. Luo, P. Zhong, J. Yao, Thermal memory based photoacoustic imaging of temperature, Optica 6 (2) (2019) 198–205.

[50] M. Fonseca, L. An, P. Beard, B. Cox, Sulfates as chromophores for multi-wavelength photoacoustic imaging phantoms, J. Biomed. Opt. 22 (12) (2017) 125007.

[51] I.G. Calasso, W. Craig, G.J. Diebold, Photoacoustic point source, Phys. Rev. Lett. 86 (16) (2001) 3550.

[52] Y.-S. Chen, W. Frey, S. Aglyamov, S. Emelianov, Environment-dependent generation of photoacoustic waves from plasmonic nanoparticles, Small (Weinh. an der Bergstr. Germany) 8 (1) (2011) 47.

[53] G.A. Pang, J. Laufer, R. Niessner, C. Haisch, Photoacoustic signal generation in gold nanospheres in aqueous solution: signal generation enhancement and particle diameter effects, J. Phys. Chem. C 120 (48) (2016) 27646–27656.

[54] F. Triki, M. Vauthrin, Mathematical modeling of the photoacoustic effect generated by the heating of metallic nanoparticles, Quart. Appl. Math. 76 (4) (2018) 673–698.

[55] E. Petrova, A. Liopo, A.A. Oraevsky, S.A. Ermilov, Temperature-dependent optoacoustic response and transient through zero Grüneisen parameter in optically contrasted media, Photoacoustics 7 (2017) 36–46, http://dx.doi.org/10.1016/j.pacs.2017.06.002, URL https://www.sciencedirect.com/science/article/pii/S2213597916300714.

[56] M.A. Anastasio, J. Zhang, X. Pan, Y. Zou, G. Ku, L.V. Wang, Half-time image reconstruction in thermoacoustic tomography, IEEE Trans. Med. Imaging 24 (2) (2005) 199–210.

[57] B.E. Treeby, T.K. Varslot, E.Z. Zhang, J.G. Laufer, P.C. Beard, Automatic sound speed selection in photoacoustic image reconstruction using an autofocus approach, J. Biomed. Opt. 16 (9) (2011) 090501.

[58] C. Yoon, J. Kang, S. Han, Y. Yoo, T.-K. Song, J.H. Chang, Enhancement of photoacoustic image quality by sound speed correction: ex vivo evaluation, Opt. Express 20 (3) (2012) 3082–3090.

[59] B. Cong, K. Kondo, T. Namita, M. Yamakawa, T. Shiina, Photoacoustic image quality enhancement by estimating mean sound speed based on optimum focusing, Japan. J. Appl. Phys. 54 (7S1) (2015) 07HC13.

[60] Y. Zhang, L. Wang, Video-rate full-ring ultrasound and photoacoustic computed tomography with real-time sound speed optimization, Biomed. Opt. Express 13 (8) (2022) 4398–4413.

[61] E. Merčep, J.L. Herraiz, X.L. Deán-Ben, D. Razansky, Transmission–reflection optoacoustic ultrasound (TROPUS) computed tomography of small animals, Light.: Sci. Appl. 8 (1) (2019) 18.

[62] W.A. Simson, M. Paschali, V. Sideri-Lampretsa, N. Navab, J.J. Dahl, Investigating pulse-echo sound speed estimation in breast ultrasound with deep learning, Ultrasonics 137 (2024) 107179.

[63] M. Suhonen, F. Lucka, A. Pulkkinen, S. Arridge, B. Cox, T. Tarvainen, Reconstructing initial pressure and speed of sound distributions simultaneously in photoacoustic tomography, 2025, arXiv preprint arXiv:2505.08482.

[64] T.R. Else, L. Hacker, J. Gröhl, E.V. Bunce, R. Tao, S.E. Bohndiek, Effects of skin tone on photoacoustic imaging and oximetry, J. Biomed. Opt. 29 (S1) (2024) S11506.

[65] T.R. Else, C. Loreno, A. Groves, B.T. Cox, J. Gröhl, I. Modolell, S.E. Bohndiek, A. Roshan, The confounding effects of skin colour in photoacoustic imaging, 2025, http://dx.doi.org/10.1101/2025.03.28.25324605, MedRxiv arXiv:https://www.medrxiv.org/content/early/2025/03/30/2025.03.28.25324605.full.pdf URL https://www.medrxiv.org/content/early/2025/03/30/2025.03.28.25324605.

[66] M.K.A. Singh, W. Steenbergen, Photoacoustic-guided focused ultrasound (pafUSion) for identifying reflection artifacts in photoacoustic imaging, Photoacoustics 3 (4) (2015) 123–131.

[67] S. Preisser, G. Held, H.G. Akarçay, M. Jaeger, M. Frenz, Study of clutter origin in in-vivo epi-optoacoustic imaging of human forearms, J. Opt. 18 (9) (2016) 094003, http://dx.doi.org/10.1088/2040-8978/18/9/094003.

[68] B.E. Treeby, Acoustic attenuation compensation in photoacoustic tomography using time-variant filtering, J. Biomed. Opt. 18 (3) (2013) 036008, http://dx.doi.org/10.1117/1.JBO.18.3.036008.

[69] J. Yang, S. Choi, C. Kim, Practical review on photoacoustic computed tomography using curved ultrasound array transducer, Biomed. Eng. Lett. (2022) 1–17.

[70] S. Guan, A.A. Khan, S. Sikdar, P.V. Chitnis, Limited-view and sparse photoacoustic tomography for neuroimaging with deep learning, Sci. Rep. 10 (1) (2020) 8510.

[71] J. Joseph, M.R. Tomaszewski, I. Quiros-Gonzalez, J. Weber, J. Brunker, S.E. Bohndiek, Evaluation of precision in optoacoustic tomography for preclinical imaging in living subjects, J. Nucl. Med. 58 (5) (2017) 807–814.

[72] L. Tan, J. Zschüntzsch, S. Meyer, A. Stobbe, H. Bruex, A.P. Regensburger, M. Claßen, F. Alves, J. Jüngert, U. Rother, et al., Non-invasive optoacoustic imaging of glycogen-storage and muscle degeneration in late-onset pompe disease, Nat. Commun. 15 (1) (2024) 7843.

[73] G.L. Menezes, R.M. Pijnappel, C. Meeuwis, R. Bisschops, J. Veltman, P.T. Lavin, M.J. Van De Vijver, R.M. Mann, Downgrading of breast masses suspicious for cancer by using optoacoustic breast imaging, Radiology 288 (2) (2018) 355–365.

[74] R. Ellwood, O. Ogunlade, E. Zhang, P. Beard, B. Cox, Photoacoustic tomography using orthogonal Fabry–Pérot sensors, J. Biomed. Opt. 22 (4) (2017) 041009.

[75] S.M. Schoustra, B. De Santi, T.J. op't Root, C.A. Klazen, M. van der Schaaf, J. Veltman, W. Steenbergen, S. Manohar, Imaging breast malignancies with the twente photoacoustic mammoscope 2, Plos One 18 (3) (2023) e0281434.

[76] S.K. Kalva, X.L. Deán-Ben, M. Reiss, D. Razansky, Spiral volumetric optoacoustic tomography for imaging whole-body biodynamics in small animals, Nat. Protoc. 18 (7) (2023) 2124–2142.

[77] L. Hacker, E.L. Brown, T.L. Lefebvre, P.W. Sweeney, S.E. Bohndiek, Performance evaluation of mesoscopic photoacoustic imaging, Photoacoustics 31 (2023) 100505.

[78] J. Yao, L.V. Wang, Photoacoustic microscopy, Laser & Photonics Rev. 7 (5) (2013) 758–778.

[79] Y. Xu, L.V. Wang, G. Ambartsoumian, P. Kuchment, Reconstructions in limited-view thermoacoustic tomography, Med. Phys. 31 (4) (2004) 724–733.

[80] G. Paltauf, R. Nuster, M. Haltmeier, P. Burgholzer, Experimental evaluation of reconstruction algorithms for limited view photoacoustic tomography with line detectors, Inverse Problems 23 (6) (2007) S81.

[81] B. Huang, J. Xia, K. Maslov, L.V. Wang, Improving limited-view photoacoustic tomography with an acoustic reflector, J. Biomed. Opt. 18 (11) (2013) 110505.

[82] D. Cai, G. Li, D. Xia, Z. Li, Z. Guo, S.-L. Chen, Synthetic aperture focusing technique for photoacoustic endoscopy, Opt. Express 25 (17) (2017) 20162–20171, http://dx.doi.org/10.1364/OE.25.020162, URL https://opg.optica.org/oe/abstract.cfm?URI=oe-25-17-20162.

[83] W. Choi, E.-Y. Park, S. Jeon, C. Kim, Clinical photoacoustic imaging platforms, Biomed. Eng. Lett. 8 (2018) 139–155.

[84] X. Liu, D. Peng, X. Ma, W. Guo, Z. Liu, D. Han, X. Yang, J. Tian, Limited-view photoacoustic imaging based on an iterative adaptive weighted filtered backprojection approach, Appl. Opt. 52 (15) (2013) 3477–3483.

[85] F. Ozdemir, B. Lafci, X.L. Dean-Ben, D. Razansky, F. Perez-Cruz, OADAT: Experimental and synthetic clinical optoacoustic data for standardized image processing, 2022, arXiv preprint arXiv:2206.08612.

[86] M. Huang, W. Liu, G. Sun, C. Shi, X. Liu, K. Han, S. Liu, Z. Wang, Z. Xie, Q. Guo, Unveiling precision: a data-driven approach to enhance photoacoustic imaging with sparse data, Biomed. Opt. Express 15 (1) (2023) 28–43.

[87] Y. Paul, D. Barthez, R. Léveillé, V. Peter, D. Scrivani, Side lobes and grating lobes artifacts in ultrasound imaging, Vet. Radiol. & Ultrasound 38 (5) (1997) 387–393.

[88] Y. Zhang, Y. Wang, C. Zhang, Total variation based gradient descent algorithm for sparse-view photoacoustic image reconstruction, Ultrasonics 52 (8) (2012) 1046–1055.

[89] Y. Xiao, Y. Shen, S. Liao, B. Yao, X. Cai, Y. Zhang, F. Gao, Limited-view photoacoustic imaging reconstruction via high-quality self-supervised neural representation, Photoacoustics (2025) 100685.

[90] N. Davoudi, X.L. Deán-Ben, D. Razansky, Deep learning optoacoustic tomography with sparse data, Nat. Mach. Intell. 1 (10) (2019) 453–460.

[91] B. Cox, B. Treeby, Effect of sensor directionality on photoacoustic imaging: a study using the k-wave toolbox, in: Photons Plus Ultrasound: Imaging and Sensing 2010, vol. 7564, SPIE, 2010, pp. 123–128.

[92] P. Warbal, R.K. Saha, In silico evaluation of the effect of sensor directivity on photoacoustic tomography imaging, Optik 252 (2022) 168305.

[93] G. Paltauf, P. Hartmair, G. Kovachev, R. Nuster, Piezoelectric line detector array for photoacoustic tomography, Photoacoustics 8 (2017) 28–36.

[94] H. Nyquist, Certain topics in telegraph transmission theory, Trans. Am. Inst. Electr. Eng. 47 (2) (1928) 617–644.

[95] J.K. Gamelin, A. Aguirre, Q. Zhu, Fast, limited-data photoacoustic imaging for multiplexed systems using a frequency-domain estimation technique, Med. Phys. 38 (3) (2011) 1503–1518.

[96] S. Arridge, P. Beard, M. Betcke, B. Cox, N. Huynh, F. Lucka, O. Ogunlade, E. Zhang, Accelerated high-resolution photoacoustic tomography via compressed sensing, Phys. Med. Biol. 61 (24) (2016) 8908.

[97] N.A. Rejesh, H. Pullagurla, M. Pramanik, Deconvolution-based deblurring of reconstructed images in photoacoustic/thermoacoustic tomography, J. Opt. Soc. Amer. A 30 (10) (2013) 1994–2001.

[98] D. Van de Sompel, L.S. Sasportas, J.V. Jokerst, S.S. Gambhir, Comparison of deconvolution filters for photoacoustic tomography, PloS One 11 (3) (2016) e0152597.

[99] Y. Wang, D. Xing, Y. Zeng, Q. Chen, Photoacoustic imaging with deconvolution algorithm, Phys. Med. Biol. 49 (14) (2004) 3117.

[100] S. Gutta, V.S. Kadimesetty, S.K. Kalva, M. Pramanik, S. Ganapathy, P.K. Yalavarthy, Deep neural network-based bandwidth enhancement of photoacoustic data, J. Biomed. Opt. 22 (11) (2017) 116001.

[101] I. Munjal, J. Prakash, Deep-learning based deconvolution for correcting spatial impulse response of transducer in optoacoustic tomography, IEEE Trans. Instrum. Meas. (2024).

[102] A.M. Winkler, K. Maslov, L.V. Wang, Noise-equivalent sensitivity of photoacoustics, J. Biomed. Opt. 18 (9) (2013) 097003.

[103] M. Welvaert, Y. Rosseel, On the definition of signal-to-noise ratio and contrast-to-noise ratio for fMRI data, PloS One 8 (11) (2013) e77089.

[104] K.M. Kempski, M.T. Graham, M.R. Gubbi, T. Palmer, M.A. Lediju Bell, Application of the generalized contrast-to-noise ratio to assess photoacoustic image quality, Biomed. Opt. Express 11 (7) (2020) 3684–3698.

[105] T. Hu, Z. Huang, P. Ge, F. Gao, F. Gao, Adaptive denoising of photoacoustic signal and image based on modified Kalman filter, J. Biophotonics 16 (5) (2023) e202200362.

[106] S. Tzoumas, A. Rosenthal, C. Lutzweiler, D. Razansky, V. Ntziachristos, Spatiospectral denoising framework for multispectral optoacoustic imaging based on sparse signal representation, Med. Phys. 41 (11) (2014) 113301.

[107] S.H. Holan, J.A. Viator, Automated wavelet denoising of photoacoustic signals for circulating melanoma cell detection and burn image reconstruction, Phys. Med. Biol. 53 (12) (2008) N227.

[108] L. Lin, P. Hu, J. Shi, C.M. Appleton, K. Maslov, L. Li, R. Zhang, L.V. Wang, Single-breath-hold photoacoustic computed tomography of the breast, Nat. Commun. 9 (1) (2018) http://dx.doi.org/10.1038/s41467-018-04576-z.

[109] W. Lee, General principles of carotid Doppler ultrasonography, Ultrasonography 33 (1) (2013) 11–17, http://dx.doi.org/10.14366/usg.13018.

[110] M. Schwarz, J. Aguirre, M. Omar, V. Ntziachristos, Chapter 26 - optoacoustic imaging of skin, in: M.R. Hamblin, P. Avci, G.K. Gupta (Eds.), Imaging in Dermatology, Academic Press, Boston, 2016, pp. 375–385, http://dx.doi.org/10.1016/B978-0-12-802838-4.00026-1, URL https://www.sciencedirect.com/science/article/pii/B9780128028384000261.

[111] A. Ron, N. Davoudi, X.L. Deán-Ben, D. Razansky, Self-gated respiratory motion rejection for optoacoustic tomography, Appl. Sci. 9 (13) (2019) http://dx.doi.org/10.3390/app9132737, URL https://www.mdpi.com/2076-3417/9/13/2737.

[112] T. Kirchner, J. Gröhl, F. Sattler, M.S. Bischoff, A. Laha, M. Nolden, L. Maier-Hein, An open-source software platform for translational photoacoustic research and its application to motion-corrected blood oxygenation estimation, 2019, arXiv preprint arXiv:1901.09781.

[113] S.J. Ford, P.L. Bigliardi, T.C.P. Sardella, A. Urich, N.C. Burton, M. Kacprowicz, M. Bigliardi, M. Olivo, D. Razansky, Structural and functional analysis of intact hair follicles and pilosebaceous units by volumetric multispectral optoacoustic tomography, J. Invest. Dermatol. 136 (4) (2016) 753–761, http://dx.doi.org/10.1016/j.jid.2015.09.001.

[114] H. He, C. Schönmann, M. Schwarz, B. Hindelang, A. Berezhnoi, S.A. Steimle-Grauer, U. Darsow, J. Aguirre, V. Ntziachristos, Fast raster-scan optoacoustic mesoscopy enables assessment of human melanoma microvasculature in vivo, Nat. Commun. 13 (1) (2022) 2803.

[115] L. Hacker, A.M. Ivory, J. Joseph, J. Gröhl, B. Zeqiri, S. Rajagopal, S.E. Bohndiek, A stable phantom material for optical and acoustic imaging, JoVE: J. Vis. Exp. 196 (2023) e65475.

[116] M. Xu, L.V. Wang, Universal back-projection algorithm for photoacoustic computed tomography, Phys. Rev. E- Stat. Nonlinear, Soft Matter Phys. 71 (1) (2005) 016706.

[117] L.A. Kunyansky, Explicit inversion formulae for the spherical mean radon transform, Inverse Problems 23 (1) (2007) 373.

[118] V. Perrot, M. Polichetti, F. Varray, D. Garcia, So you think you can DAS? A viewpoint on delay-and-sum beamforming, Ultrasonics 111 (2021) 106309.

[119] G. Matrone, A.S. Savoia, G. Caliano, G. Magenes, The delay multiply and sum beamforming algorithm in ultrasound B-mode medical imaging, IEEE Trans. Med. Imaging 34 (4) (2014) 940–949.

[120] M. Jaeger, S. Schüpbach, A. Gertsch, M. Kitz, M. Frenz, Fourier reconstruction in optoacoustic imaging using truncated regularized inverse k-space interpolation, Inverse Problems 23 (6) (2007) S51.

[121] D. Finch, S.K. Patch, Rakesh, Determining a function from its mean values over a family of spheres, SIAM J. Math. Anal. 35 (5) (2004) 1213–1240.

[122] P. Burgholzer, G.J. Matt, M. Haltmeier, G. Paltauf, Exact and approximative imaging methods for photoacoustic tomography using an arbitrary detection surface, Phys. Rev. E— Stat. Nonlinear, Soft Matter Phys. 75 (4) (2007) 046706.

[123] Y. Hristova, P. Kuchment, L. Nguyen, Reconstruction and time reversal in thermoacoustic tomography in acoustically homogeneous and inhomogeneous media, Inverse Problems 24 (5) (2008) 055006.

[124] M. Agranovsky, P. Kuchment, Uniqueness of reconstruction and an inversion procedure for thermoacoustic and photoacoustic tomography with variable sound speed, Inverse Problems 23 (5) (2007) 2089.

[125] P. Stefanov, G. Uhlmann, Thermoacoustic tomography with variable sound speed, Inverse Problems 25 (7) (2009) 075011.

[126] J. Qian, P. Stefanov, G. Uhlmann, H. Zhao, An efficient Neumann series–based algorithm for thermoacoustic and photoacoustic tomography with variable sound speed, SIAM J. Imaging Sci. 4 (3) (2011) 850–883.

[127] K. Wang, R. Su, A.A. Oraevsky, M.A. Anastasio, Investigation of iterative image reconstruction in three-dimensional optoacoustic tomography, Phys. Med. Biol. 57 (17) (2012) 5399.

[128] B. Cox, P.C. Beard, Modeling photoacoustic propagation in tissue using k-space techniques, in: Photoacoustic Imaging and Spectroscopy, CRC Press, 2017, pp. 25–34.

[129] A. Hauptmann, F. Lucka, M. Betcke, N. Huynh, J. Adler, B. Cox, P. Beard, S. Ourselin, S. Arridge, Model-based learning for accelerated, limited-view 3-D photoacoustic tomography, IEEE Trans. Med. Imaging 37 (6) (2018) 1382–1393.

[130] D. Waibel, J. Gröhl, F. Isensee, T. Kirchner, K. Maier-Hein, L. Maier-Hein, Reconstruction of initial pressure from limited view photoacoustic images using deep learning, in: Photons Plus Ultrasound: Imaging and Sensing 2018, vol. 10494, SPIE, 2018, pp. 196–203.

[131] M. Kim, G.-S. Jeng, I. Pelivanov, M. O'Donnell, Deep-learning image reconstruction for real-time photoacoustic system, IEEE Trans. Med. Imaging 39 (11) (2020) 3379–3390.

[132] X.L. Deán-Ben, A. Özbek, D. Razansky, Accounting for speed of sound variations in volumetric hand-held optoacoustic imaging, Front. Optoelectron. 10 (2017) 280–286.

[133] T. Yue, W. Jiang, Y. Luo, H. Song, X. Wang, H. Deng, C. Ma, Double speed-of-sound photoacoustic image reconstruction at 10 frames-per-second with automatic segmentation, in: Optics in Health Care and Biomedical Optics XII, vol. 12320, SPIE, 2022, pp. 164–171.

[134] J. Jose, R.G. Willemink, W. Steenbergen, C.H. Slump, T.G. van Leeuwen, S. Manohar, Speed-of-sound compensated photoacoustic tomography for accurate imaging, Med. Phys. 39 (12) (2012) 7262–7271.

[135] J. Xia, C. Huang, K. Maslov, M.A. Anastasio, L.V. Wang, Enhancement of photoacoustic tomography by ultrasonic computed tomography based on optical excitation of elements of a full-ring transducer array, Opt. Lett. 38 (16) (2013) 3140–3143.

[136] G. Wurzinger, R. Nuster, G. Paltauf, Combined photoacoustic, pulse-echo laser ultrasound, and speed-of-sound imaging using integrating optical detection, J. Biomed. Opt. 21 (8) (2016) 086010.

[137] M. Dantuma, F. Lucka, S. Kruitwagen, A. Javaherian, L. Alink, R. van Meerdervoort, M. Nanninga, T. Root, B. De Santi, J. Budisky, et al., Fully three-dimensional sound speed-corrected multi-wavelength photoacoustic breast tomography, 2023, arXiv preprint arXiv:2308.06754.

[138] Z. Belhachmi, T. Glatz, O. Scherzer, A direct method for photoacoustic tomography with inhomogeneous sound speed, Inverse Problems 32 (4) (2016) 045005.

[139] J. Tick, A. Pulkkinen, T. Tarvainen, Modelling of errors due to speed of sound variations in photoacoustic tomography using a Bayesian framework, Biomed. Phys. Eng. Express 6 (1) (2019) 015003.

[140] J. Zhang, M.A. Anastasio, Reconstruction of speed-of-sound and electromagnetic absorption distributions in photoacoustic tomography, in: Photons Plus Ultrasound: Imaging and Sensing 2006: The Seventh Conference on Biomedical Thermoacoustics, Optoacoustics, and Acousto-Optics, vol. 6086, SPIE, 2006, pp. 339–345.

[141] M. Cui, H. Zuo, X. Wang, K. Deng, J. Luo, C. Ma, Adaptive photoacoustic computed tomography, Photoacoustics 21 (2021) 100223.

[142] T.P. Matthews, M.A. Anastasio, Joint reconstruction of the initial pressure and speed of sound distributions from combined photoacoustic and ultrasound tomography measurements, Inverse Problems 33 (12) (2017) 124002.

[143] J. Poudel, M.A. Anastasio, Joint reconstruction of initial pressure distribution and spatial distribution of acoustic properties of elastic media with application to transcranial photoacoustic tomography, Inverse Problems 36 (12) (2020) 124007.

[144] G. Jeong, U. Villa, M.A. Anastasio, Revisiting the joint estimation of initial pressure and speed-of-sound distributions in photoacoustic computed tomography with consideration of canonical object constraints, Photoacoustics (2025) 100700.

[145] A.F. Frangi, W.J. Niessen, K.L. Vincken, M.A. Viergever, Multiscale vessel enhancement filtering, in: Medical Image Computing and Computer-Assisted Intervention—MICCAI'98: First International Conference Cambridge, MA, USA, October 11–13, 1998 Proceedings 1, Springer, 1998, pp. 130–137.

[146] S. Mandal, M. Mueller, D. Komljenovic, Multimodal priors reduce acoustic and optical inaccuracies in photoacoustic imaging, in: Photons Plus Ultrasound: Imaging and Sensing 2019, vol. 10878, SPIE, 2019, pp. 103–107.

[147] H. Yang, D. Jüstel, J. Prakash, A. Karlas, A. Helfen, M. Masthoff, M. Wildgruber, V. Ntziachristos, Soft ultrasound priors in optoacoustic reconstruction: Improving clinical vascular imaging, Photoacoustics 19 (2020) 100172.

[148] Y. Zhao, C. Zhang, S. Liu, C. Tian, Ultrasound-guided adaptive photoacoustic tomography, Opt. Lett. 47 (15) (2022) 3960–3963.

[149] L.I. Rudin, S. Osher, E. Fatemi, Nonlinear total variation based noise removal algorithms, Phys. D: Nonlinear Phenom. 60 (1–4) (1992) 259–268.

[150] L. Yao, H. Jiang, Enhancing finite element-based photoacoustic tomography using total variation minimization, Appl. Opt. 50 (25) (2011) 5031–5041.

[151] N. Parikh, S. Boyd, et al., Proximal algorithms, Found. Trends® Optim. 1 (3) (2014) 127–239.

[152] Y.E. Boink, M.J. Lagerwerf, W. Steenbergen, S.A. van Gils, S. Manohar, C. Brune, A reconstruction framework for total generalised variation in photoacoustic tomography, 2017, arXiv e-prints.

[153] A. Hauptmann, B. Cox, Deep learning in photoacoustic tomography: current approaches and future directions, J. Biomed. Opt. 25 (11) (2020) 112903.

[154] J. Gröhl, M. Schellenberg, K. Dreher, L. Maier-Hein, Deep learning for biomedical photoacoustic imaging: A review, Photoacoustics 22 (2021) 100241.

[155] H. Deng, H. Qiao, Q. Dai, C. Ma, Deep learning in photoacoustic imaging: a review, J. Biomed. Opt. 26 (4) (2021) 040901.

[156] C. Yang, H. Lan, F. Gao, F. Gao, Review of deep learning for photoacoustic imaging, Photoacoustics 21 (2021) 100215.

[157] P. Rajendran, A. Sharma, M. Pramanik, Photoacoustic imaging aided with deep learning: a review, Biomed. Eng. Lett. (2022) 1–19.

[158] J. Yang, S. Choi, J. Kim, B. Park, C. Kim, Recent advances in deep-learning-enhanced photoacoustic imaging, Adv. Photonics Nexus 2 (5) (2023) 054001.

[159] X. Wei, T. Feng, Q. Huang, Q. Chen, C. Zuo, H. Ma, Deep learning-powered biomedical photoacoustic imaging, Neurocomputing 573 (2024) 127207.

[160] Y. Wang, D. Xing, Y. Zeng, Q. Chen, Photoacoustic imaging with deconvolution algorithm, Phys. Med. Biol. 49 (14) (2004) 3117, http://dx.doi.org/10.1088/0031-9155/49/14/006.

[161] L. Qi, J. Wu, X. Li, S. Zhang, S. Huang, Q. Feng, W. Chen, Photoacoustic tomography image restoration with measured spatially variant point spread functions, IEEE Trans. Med. Imaging 40 (9) (2021) 2318–2328, http://dx.doi.org/10.1109/TMI.2021.3077022.

[162] K. Kratkiewicz, A. Pattyn, N. Alijabbari, M. Mehrmohammadi, Ultrasound and photoacoustic imaging of breast cancer: clinical systems, challenges, and future outlook, J. Clin. Med. 11 (5) (2022) 1165.

[163] M.K. Feldman, S. Katyal, M.S. Blackwood, US artifacts, RadioGraphics 29 (4) (2009) 1179–1189, http://dx.doi.org/10.1148/rg.294085199, PMID: 19605664.

[164] J. Bamber, C. Hill, Acoustic properties of normal and cancerous human liver—I. Dependence on pathological condition, Ultrasound Med. Biol. 7 (2) (1981) 121–133.

[165] B.D. Santi, L. Kim, R.F.G. Bulthuis, F. Lucka, S. Manohar, Automated three-dimensional image registration for longitudinal photoacoustic imaging, J. Biomed. Opt. 29 (S1) (2024) S11515, http://dx.doi.org/10.1117/1.JBO.29.S1.S11515.

[166] M.C. Ziskin, D.I. Thickman, N.J. Goldenberg, M.S. Lapayowker, J.M. Becker, The comet tail artifact., J. Ultrasound Med. 1 (1) (1982) 1–7, http://dx.doi.org/10.7863/jum.1982.1.1.1, arXiv:https://onlinelibrary.wiley.com/doi/pdf/10.7863/jum.1982.1.1.1 URL https://onlinelibrary.wiley.com/doi/abs/10.7863/jum.1982.1.1.1.

[167] D. Park, E.-A. Park, B. Jeong, Y.S. Lee, W. Lee, Quantitative analysis of blooming artifact caused by calcification based on X-ray energy difference using computed tomography, Sci. Rep. 14 (1) (2024) 11539, http://dx.doi.org/10.1038/s41598-024-61187-z.

[168] H.N.Y. Nguyen, W. Steenbergen, Reducing artifacts in photoacoustic imaging by using multi-wavelength excitation and transducer displacement, Biomed. Opt. Express 10 (7) (2019) 3124–3138, http://dx.doi.org/10.1364/BOE.10.003124, URL https://opg.optica.org/boe/abstract.cfm?URI=boe-10-7-3124.

[169] B.D. Santi, F. Lucka, R. Bulthuis, J. Veltman, M. van der Schaaf, H. Messal, M. Brinkhuis, B. Cox, S. Manohar, Image analysis of patient data from the hybrid photoacoustic-ultrasound tomography system PAM3, in: A.A. Oraevsky, L.V. Wang (Eds.), in: Photons Plus Ultrasound: Imaging and Sensing 2025, vol. 13319, SPIE, 2025, 1331902, http://dx.doi.org/10.1117/12.3043362.

[170] K. Shen, K. Niu, S. Liu, Y.M. Paulus, X. Jiang, C. Tian, Physics-driven deep learning photoacoustic tomography, Fundam. Res. (2024) http://dx.doi.org/10.1016/j.fmre.2024.06.014, URL https://www.sciencedirect.com/science/article/pii/S2667325824003583.

[171] C. Tian, K. Shen, W. Dong, F. Gao, K. Wang, J. Li, S. Liu, T. Feng, C. Liu, C. Li, M. Yang, S. Wang, J. Tian, Image reconstruction from photoacoustic projections, Photonics Insights 3 (3) (2024) R06, http://dx.doi.org/10.3788/PI.2024.R06.

[172] C. Tian, C. Zhang, H. Zhang, D. Xie, Y. Jin, Spatial resolution in photoacoustic computed tomography, Rep. Progr. Phys. 84 (3) (2021) 036701, http://dx.doi.org/10.1088/1361-6633/abdab9.

[173] C. Cai, X. Wang, K. Si, J. Qian, J. Luo, C. Ma, Streak artifact suppression in photoacoustic computed tomography using adaptive back projection, Biomed. Opt. Express 10 (9) (2019) 4803–4814, http://dx.doi.org/10.1364/BOE.10.004803, URL https://opg.optica.org/boe/abstract.cfm?URI=boe-10-9-4803.

[174] T. Oruganti, J.G. Laufer, B.E. Treeby, Vessel filtering of photoacoustic images, in: A.A. Oraevsky, L.V. Wang (Eds.), in: Photons Plus Ultrasound: Imaging and Sensing 2013, vol. 8581, SPIE, 2013, p. 85811W, http://dx.doi.org/10.1117/12.2005988.

[175] A. Longo, S. Morscher, J.M. Najafababdi, D. Jüstel, C. Zakian, V. Ntziachristos, Assessment of hessian-based frangi vesselness filter in optoacoustic imaging, Photoacoustics 20 (2020) 100200, http://dx.doi.org/10.1016/j.pacs.2020.100200, URL https://www.sciencedirect.com/science/article/pii/S2213597920300409.

Max Rietberg completed his Master's degrees in Biomedical Engineering and Computer Science at the University of Twente, the Netherlands, as part of the Biomedical Photonic Imaging research group. Currently, he is a Ph.D. candidate in the Multi-Modality Medical Imaging research group at the University of Twente, focusing on the optimization of photoacoustic imaging through simulations.